












First Resolution of Microlensed Images of a Binary-Lens Event

ZEXUAN WU ^{1,2} SUBO DONG ^{1,2,3} A. MÉRAND ⁴ CHRISTOPHER S. KOCHANÉK,^{5,6}
PRZEMEK MRÓZ ⁷ JINYI SHANGGUAN,⁸ GRANT CHRISTIE,⁹ THIAM-GUAN TAN ¹⁰
THOMAS BENSBY ¹¹ JOSS BLAND-HAWTHORN ^{12,13} SVEN BUDER ^{14,13} FRANK EISENHAEUER,^{8,15}
ANDREW P. GOULD,^{16,5} JANEZ KOS ¹⁷ TIM NATUSCH,^{18,9} SANJIB SHARMA ^{12,13}
ANDRZEJ UDALSKI ⁷ J. WOILLEZ,⁴ DAVID A. H. BUCKLEY¹⁹ AND I. B. THOMPSON²⁰

KARIM ABD EL DAYEM,²¹ ANTHONY BERDEU,²¹ JEAN-PHILIPPE BERGER,²²
GUILLAUME BOURDAROT,⁸ WOLFGANG BRANDNER,¹⁶ RICHARD I. DAVIES,⁸ DENIS DEFRÈRE,²³
CATHERINE DOUGADOS,²² ANTONIA DRESCHER,⁸ ANDREAS ECKART,^{24,25} MAXIMILIAN FABRICIUS,⁸
HELMUT FEUCHTGRUBER,⁸ NATASCHA M. FÖRSTER SCHREIBER,⁸ PAULO GARCIA,^{26,27}
REINHARD GENZEL,^{8,28} STEFAN GILLESSEN,⁸ GERNOT HEIßEL,²¹ SEBASTIAN HÖNIG,²⁹
MATHIS HOULLE,³⁰ PIERRE KERVELLA,²¹ LAURA KREIDBERG,¹⁶ SYLVESTRE LACOUR,^{21,4}
OLIVIER LAI,³⁰ ROMAIN LAUGIER,²³ JEAN-BAPTISTE LE BOUQUIN,²² JAMES LEFTLEY,³⁰
BRUNO LOPEZ,³⁰ DIETER LUTZ,⁸ FELIX MANG,⁸ FLORENTIN MILLOUR,³⁰ MIGUEL MONTARGÈS,²¹
HUGO NOWACKI,²² MATHIAS NOWAK,²¹ THOMAS OTT,⁸ THIBAUT PAUMARD,²¹ KARINE PERRAUT,²²
GUY PERRIN,²¹ ROMAIN PETROV,³⁰ PIERRE-OLIVIER PETRUCCI,²² NICOLAS POURRE,²²
SEBASTIAN RABIEN,⁸ DIOGO C. RIBEIRO,⁸ SYLVIE ROBBE-DUBOIS,³⁰ MATTEO SADUN BORDONI,⁸
DARYL SANTOS,⁸ JONAS SAUTER,¹⁶ JULES SCIGLIUTO,³⁰ TARO T. SHIMIZU,⁸
CHRISTIAN STRAUBMEIER,²⁴ ECKHARD STURM,⁸ MATTHIAS SUBROWIT,²⁴ CALVIN SYKES,²⁹
LINDA TACCONI,⁸ FRÉDÉRIC VINCENT,²¹ FELIX WIDMANN,⁸
(THE GRAVITY+ COLLABORATION)

¹Department of Astronomy, School of Physics, Peking University, 5 Yiheyuan Road, Haidian District, Beijing 100871, People's Republic of China

²Kavli Institute of Astronomy and Astrophysics, Peking University, 5 Yiheyuan Road, Haidian District, Beijing 100871, People's Republic of China

³National Astronomical Observatories, Chinese Academy of Science, 20A Datun Road, Chaoyang District, Beijing 100101, People's Republic of China

⁴European Southern Observatory, Karl-Schwarzschild-Straße 2, D-85748 Garching, Germany

⁵Department of Astronomy, Ohio State University, 140 W. 18th Ave., Columbus, OH 43210, USA

⁶Center for Cosmology and AstroParticle Physics (CCAPP), The Ohio State University, 191 W. Woodruff Avenue, Columbus, OH 43210, USA.

⁷Astronomical Observatory, University of Warsaw, Al. Ujazdowskie 4, 00-478 Warszawa, Poland

⁸Max Planck Institute for Extraterrestrial Physics, Giessenbachstraße 1, D-85748 Garching, Germany

⁹Auckland Observatory, Auckland, New Zealand

¹⁰Perth Exoplanet Survey Telescope, Perth, Australia

¹¹Lund Observatory, Division of Astrophysics, Department of Physics, Lund University, Box 118, SE-22100 Lund, Sweden

¹²Sydney Institute for Astronomy, School of Physics, A28, The University of Sydney, NSW 2006, Australia

- ¹³*ARC Centre of Excellence for All Sky Astrophysics in 3 Dimensions (ASTRO 3D), Australia*
- ¹⁴*Research School of Astronomy and Astrophysics, The Australian National University, Canberra ACT2611, Australia*
- ¹⁵*Department of Physics, Technical University of Munich, 85748 Garching, Germany*
- ¹⁶*Max Planck Institute for Astronomy, Königstuhl 17, 69117 Heidelberg, Germany*
- ¹⁷*Faculty of Mathematics and Physics, University of Ljubljana, Jadranska 19, 1000 Ljubljana, Slovenia*
- ¹⁸*Mathematical Sciences Department, Auckland University of Technology, Auckland, New Zealand*
- ¹⁹*South African Astronomical Observatory, P.O. Box 9, Observatory 7935, Cape Town, South Africa*
- ²⁰*Carnegie Observatories, 813 Santa Barbara Street, Pasadena, CA 91101-1292, USA*
- ²¹*LESIA, Observatoire de Paris, Université PSL, Sorbonne Université, Université Paris Cité, CNRS, 5 place Jules Janssen, 92195 Meudon, France*
- ²²*Univ. Grenoble Alpes, CNRS, IPAG, 38000 Grenoble, France*
- ²³*Institute of Astronomy, KU Leuven, Celestijnenlaan 200D, 3001, Leuven, Belgium*
- ²⁴*1st Institute of Physics, University of Cologne, Zùlpicher StraÙe 77, 50937 Cologne, Germany*
- ²⁵*Max Planck Institute for Radio Astronomy, Auf dem Hùgel 69, 53121 Bonn, Germany*
- ²⁶*Faculdade de Engenharia, Universidade do Porto, R. Dr. Roberto Frias s/n, 4200-465 Porto, Portugal*
- ²⁷*CENTRA – Centro de Astrofísica e Gravitação, IST, Universidade de Lisboa, 1049-001 Lisboa, Portugal*
- ²⁸*Departments of Physics and Astronomy, Le Conte Hall, University of California, Berkeley, CA 94720, USA*
- ²⁹*School of Physics & Astronomy, University of Southampton, University Road, Southampton SO17 1BJ, UK*
- ³⁰*Université Côte d’Azur, Observatoire de la Côte d’Azur, CNRS, Laboratoire Lagrange, CS 34229, F-06304 Nice cedex 4, France*

ABSTRACT

We resolve the multiple images of the binary-lens microlensing event ASASSN-22av using the GRAVITY instrument of the Very Large Telescope Interferometer (VLTI). The light curves show weak binary-lens perturbations, complicating the analysis, but the joint modeling with the VLTI data breaks several degeneracies, arriving at a strongly favored solution. Thanks to precise measurements of angular Einstein radius $\theta_E = 0.724 \pm 0.002$ mas and microlens parallax, we determine that the lens system consists of two M dwarfs with masses of $M_1 = 0.258 \pm 0.008 M_\odot$ and $M_2 = 0.130 \pm 0.007 M_\odot$, a projected separation of $r_\perp = 6.83 \pm 0.31$ au and a distance of $D_L = 2.29 \pm 0.08$ kpc. The successful VLTI observations of ASASSN-22av open up a new path for studying intermediate-separation (i.e., a few astronomical units) stellar-mass binaries, including those containing dark compact objects such as neutron stars and stellar-mass black holes.

Keywords: Gravitational microlensing (672); Binary lens microlensing(2136); Optical interferometry (1168)

1. INTRODUCTION

In recent years, the enhanced sensitivity of advanced instrumentation (Eisenhauer et al. 2023) at the Very Large Telescope Interferometer (VLTI) of the European Southern Observatory (ESO) has facilitated the interferometric resolution of microlensed images (Delplancke et al. 2001), with the first successful case achieved by Dong et al. (2019) using the GRAVITY instrument (GRAVITY Collaboration et al. 2017). By enabling direct mass determinations, interferometric microlensing

opens up a new path into studying Galactic stellar-mass systems, including dark compact objects such as neutron stars and black holes.

The observable effect of microlensing (Einstein 1936; Paczyński 1986) is the magnified flux of a background star (i.e., the “source”) due to the gravitational deflection by a foreground object (i.e., the “lens”), and thus microlensing is a sensitive probe of the mass of the lens system, irrespective of its brightness. However, the most easily extracted quantity, the Einstein timescale t_E is a degenerate combination of the lens mass M_L , the lens-source relative parallax π_{rel} and the proper motion μ_{rel} :

$$t_E = \frac{\theta_E}{\mu_{\text{rel}}}; \quad \theta_E \equiv \sqrt{\kappa M_L \pi_{\text{rel}}}; \quad \kappa \equiv \frac{4G}{c^2 \text{au}} \simeq 8.144 \frac{\text{mas}}{M_\odot}, \quad (1)$$

where θ_E is the angular Einstein radius, which is of the order of milliarcseconds for stellar-mass microlenses in the Galaxy. To break this degeneracy, a common approach is to measure both θ_E and the so-called “microlens parallax” π_E to determine the lens mass (Gould 2000, 2004):

$$M_L = \frac{\theta_E}{\kappa \pi_E}, \quad (2)$$

where π_E is a two-dimensional vector (Gould 2004) along the same direction as the lens-source relative proper motion vector μ_{rel} :

$$\pi_E \equiv \frac{\pi_{\text{rel}}}{\theta_E} \frac{\mu_{\text{rel}}}{\mu_{\text{rel}}}. \quad (3)$$

The key advantage of the interferometric microlensing method is that it yields not only precise θ_E , from measuring the angular separation of images, but also constraints on the direction of π_E .

One often obtains “one-dimensional” microlens parallax from the light curves; that is, the component of π_E parallel to the Earth’s acceleration is generally much better constrained than the perpendicular component (Gould et al. 1994; Smith et al. 2003; Gould 2004). As demonstrated by Dong et al. (2019), Zang et al. (2020), and Cassan et al. (2022), VLTI microlensing can drastically improve the π_E measurements from accurate directional constraints via measuring the position angles of images.

A long-adopted method for determining θ_E is via the “finite-source effects” (Gould 1994a), when the source transits/approaches a caustic (a set of positions that, for a point source, induce infinite magnification). Modeling the finite-source effects in the microlensing light curve measures the ratio between θ_E and the angular radius of the source star θ_* , where θ_* can be derived from the photometric properties of the source. For a single lens, the caustic is point-like, so finite-source detections in stellar single-lens events are usually restricted to rare cases reaching a high peak magnification of $A_{\text{peak}} \gtrsim 100$. In contrast, binary lenses have extended caustic structures, and thus finite-source effects manifest more often in binary-lens events. The first microlens mass measurement by An et al. (2002) is from such a caustic-crossing binary-lens event. However, this method is ineffective for studying events with weak binary-lens perturbations (e.g., non-caustic-crossing). One such weak-binary event was OGLE-2005-SMC-001, for which Dong et al. (2007) detected the space-based microlens parallax (Refsdal 1966; Gould 1994b) for the first time, and since no finite-source effects were detected, it was not possible to definitively determine the lens mass due to the absence of a θ_E measurement. While the exact fraction of weak binary-lens events is still an open question, Zhu et al. (2014) predicted and Jung et al. (2022) confirmed that half of planetary events would lack caustic crossings, despite their

continuous and high-cadence coverages, implying that weak binaries may encompass a significant fraction of binary-lens parameter space.

With milliarcsecond resolution, VLTI can resolve the microlensed images with angular separations around $\gtrsim 2\theta_E$ for a stellar-mass-lens microlensing event (Delplancke et al. 2001; Dalal & Lane 2003; Rattenbury & Mao 2006; Cassan & Ranc 2016) and then can determine θ_E at \sim percent precision. Dong et al. (2019) measured $\theta_E = 1.87 \pm 0.03$ mas for TCP J05074264+2447555 (aka Kojima-1) with VLTI GRAVITY, leading to a mass measurement of $M_L = 0.495 \pm 0.063 M_\odot$ when combined with the microlens parallax (Zang et al. 2020). Cassan et al. (2022) obtained $\theta_E = 0.7650 \pm 0.0038$ mas for Gaia19bld (Rybicki et al. 2022) with VLTI PIONIER (Le Bouquin et al. 2011b) and then determined that $M_L = 1.147 \pm 0.029 M_\odot$. Both events were exceptionally bright, since VLTI observations were limited by the instrument’s sensitivity, with $K \lesssim 10.5$ for the on-axis mode of GRAVITY and $H \lesssim 7.5$ for PIONIER. GRAVITY has recently been upgraded to enable dual-beam capability (known as “GRAVITY Wide”; GRAVITY+ Collaboration et al. 2022a) with a boosted sensitivity, and using GRAVITY wide, Mróz et al. (2024) measured that OGLE-2023-BLG-0061/KMT-2023-BLG-0496 has $\theta_E = 1.280 \pm 0.009$ mas and inferred its lens mass $M_L = 0.472 \pm 0.012 M_\odot$. Future upgrades to GRAVITY+ are expected to significantly improve the sensitivity (GRAVITY+ Collaboration et al. 2022b) and consequently the number of accessible microlensing events.

The VLTI microlensing observations published so far have been exclusively on single-lens events (or hosts of extremely low-mass companions). Here, we analyze ASASSN-22av, the *first binary-lens* microlensing event with multiple images resolved by VLTI.

2. OBSERVATIONS AND DATA REDUCTION

ASASSN-22av was discovered as a microlensing event candidate¹ on UT 2022-01-19.10 by the All-Sky Automatic Survey for Supernovae (ASAS-SN; Shappee et al. 2014). Its Gaia DR3 (Gaia Collaboration et al. 2023) `source_id` is 5887701839850363776 and coordinates are $(\alpha, \delta)_{J2000} = (15^h01^m00.66^s, -54^\circ23'59.96'')$, corresponding to Galactic coordinates $(l, b)_{J2000} = (321.^\circ14522, 3.^\circ82467)$. Following its discovery, we modeled the real-time ASAS-SN light curve² (Kochanek et al. 2017) and found that it was consistent with a point-source point-lens (PSPL; Paczyński 1986) model, reaching a peak magnification of $A_{\text{peak}} \sim 20\text{--}30$ around UT 2022 January 20. Its baseline is at $K_s = 9.27 \pm 0.02$ (Two Micron All Sky Survey or 2MASS ID: J15010066–5423599) and $G = 13.82$, and the magnified brightness was well above the limit for conducting on-axis GRAVITY observations with Multi-Application Curvature Adaptive Optics (MACAO).

We began to conduct VLTI GRAVITY observations on the night of UT 2022 January 21 and subsequently made ongoing observations until 2022 January 25. We discuss the VLTI observations and data reduction in § 2.1. We also started photometric follow-up observations on UT 2022 January 20 (see § 2.2 for detailed descriptions of photometric data). On UT 2022 January 21, our light-curve modeling suggested significant deviations from the best-fit PSPL model, and we found that a finite-source point-lens (FSPL) model was now preferred. Aiming at performing “stellar atmosphere tomography” (see, e.g., Albrow et al. 2001; Afonso et al. 2001, and references therein) near the caustic exit, we initiated a campaign of time-series high-resolution spectroscopy. On UT 2022 January 24, we noticed that the light curve declined faster than expected from the best-fit FSPL model and

¹ <https://www.astronomy.ohio-state.edu/asassn/transients.html>

² <https://asas-sn.osu.edu>

considered the possibility of a binary-lens perturbation, which was confirmed by our later analysis (see § 3 for detailed discussions on light-curve modeling). We obtained high-resolution spectra from the High Resolution Spectrograph (HRS) on the Southern African Large Telescope (SALT; Buckley et al. 2006), the MIKE spectrograph (Bernstein et al. 2003) on the Magellan Clay 6.5 m telescope, the High Efficiency and Resolution Multi Element Spectrograph (HERMES; Sheinis et al. 2015) on the Anglo-Australian Telescope (AAT), and the HARPS spectrograph (Mayor et al. 2003) on the ESO’s 3.6 m telescope, from UT 2022 January 25 to UT 2022 January 30. The full description of the spectroscopic data and the stellar atmosphere tomography analysis will be presented in a future paper. In this work, we utilize the stellar parameters of the source extracted from the HERMES data presented in § 2.3.

2.1. Interferometric Data

We observed ASASSN-22av with the GRAVITY instrument (GRAVITY Collaboration et al. 2017) and four 8 m Unit Telescopes (UTs) on the four nights of 2022 January 21, 22, 24, and 25. The observations were executed with the single-field on-axis mode at medium resolution ($R = \lambda/\Delta\lambda \simeq 500$). We use all data except those on 2022 January 21, when there was significant flux loss in UT2 and poor fringe-tracking performance. The remaining three nights of data are reduced with the standard GRAVITY pipeline (version 1.6.6), and there are two, four, and two exposures on the nights of 22, 24, and 25, respectively. Throughout this paper, we refer to these three nights as Nights 1, 2, and 3, respectively. We first use the Python script `run_gravi_reduced.py` to reduce the raw data up to the application of the pixel-to-visibility matrix (P2VM). The default options are used except for adopting `--gravity_vis.output-phase-sc=SELF_VISPHI` to calculate the internal differential phase between each spectral channel. The pipeline performed the bias and sky subtraction, flat-fielding, wavelength calibration, and spectral extraction. Application of the P2VM converts the pixel detector counts into complex visibilities, taking into account all instrumental effects, including relative throughput, coherence, phase shift, and crosstalk. The dark, bad-pixel, flat-field, wavelength calibration, and P2VM matrix data are reduced from the daily calibration data obtained close in time to our observations. We then use `run_gravi_trend.py` to calibrate the closure phase with the calibrator observation of HD 134122 next to the science target observations.

The observations employed four UTs and thus there are four closure phases for every spectral channel. In principle, the four closure phases are not independent and should sum up to zero. We examine the calibrator data and find that the standard deviation of the sum of the closure phases is $\sim 0.^{\circ}15$, comparable to the pipeline-reported closure-phase uncertainties in the science data. Thus, we take the simplified approach and treat the four closure phases as uncorrelated observables rather than the more sophisticated approach of treating the correlated noise employed by Kammerer et al. (2020). On each night, we have two exposures for the calibrator star, and we find the closure-phase differences of the two exposures have scatters of $0.^{\circ}21$, $0.^{\circ}25$, $0.^{\circ}35$ on Night 1, 2, and 3, respectively. We adopt these values as the uncertainties introduced in the calibration process and add them quadratically to the closure-phase errors.

The medium-resolution spectrograph samples 233 wavelengths spanning $2.0 - 2.4 \mu\text{m}$. To speed up computation, the 233 closure phases are binned into 10 phases in our modeling process. The first and last phases are discarded due to the low signal-to-noise ratios and significant deviations from the model. See Appendix A for the description of the binning process.

2.2. Photometric Data

We obtained follow-up imaging data taken with the 1 m telescopes of the Las Cumbres Observatory Global Telescope Network (LCOGT; [Brown et al. 2013](#)) in the Sloan $g'r'i'$ filters, the 0.4 m telescope of Auckland Observatory (AO) at Auckland (New Zealand) in the $g'r'i'$ filters, and the 30 cm Perth Exoplanet Survey Telescope (PEST) in the $g'r'i'$ filters.

We use the PmPyeasy pipeline ([Chen et al. 2022](#)) to do the photometry on these follow-up images. For LCOGT and PEST data, we conduct image subtractions with the `hotpants`³ code ([Becker 2015](#)), and then we employ aperture photometry on the subtracted images. For the AO data, we performed point-spread function (PSF) photometry using DoPHOT ([Schechter et al. 1993](#)).

We coadded and analyzed the g' -band ASAS-SN images using the standard ASAS-SN photometric pipeline based on the ISIS image-subtraction code ([Alard & Lupton 1998](#); [Alard 2000](#)). The baseline ($g' \sim 15.5$) is too faint to obtain precise photometry for ASAS-SN, and we analyze the magnified ASAS-SN epochs with $HJD' = HJD - 2450000 \in (9577.857, 9677.608)$. There are data from three ASAS-SN cameras (`be`, `bi` and `bm`), and they are analyzed independently in the modeling.

This event was announced⁴ as Gaia22ahy by Gaia Science Alerts (GSA; [Hodgkin et al. 2021](#)) on UT 2022-01-25.4. The Gaia G -band light curve available on GSA website does not have uncertainties, and we adopt the same error bar ($\sigma_G = 0.02$) for all data points. We noticed that the data in 2015 exhibit systematically larger scatter than the rest of the Gaia baseline. By inspecting a few other GSA microlensing light curves ([Wyrzykowski et al. 2023](#)), we found similar patterns at the beginning of the Gaia mission, possibly due to the continued contamination by water ice ([Gaia Collaboration et al. 2016](#)). We conservatively remove all Gaia data before the last decontamination run on 2016 August 22 ([Riello et al. 2021](#)) from our analysis.

We follow the standard procedure ([Yee et al. 2012](#)) of renormalizing the error bars such that $\chi^2/\text{degrees of freedom (dof)}$ is unity for each data set for the best-fit model. We reject the 3σ outliers and thereby exclude four out of 983 photometric data points from the analysis (the rejected data consist of one data point each from LCOGT r' and i' and one epoch each from the ASAS-SN `bi` and `bm` cameras). Figure 1 shows the multiband light curves of ASASSN-22av.

2.3. HERMES Spectroscopic Data and Stellar Parameters

We obtained a high-resolution optical spectrum (`subject_id` 220125001601051) on UT 2022-01-25.75 as part of ongoing observations of the Galactic Archaeology with HERMES survey ([De Silva et al. 2015](#)). The total exposure time is 3600 s. The HERMES spectrograph on the 3.9 m AAT at Siding Spring Observatory covers four wavelength regions (4713–4903, 5648–5873, 6478–6737, and 7585–7887 Å) that can show absorption features from up to 31 elements, including the two strong Balmer lines $H\alpha$ and $H\beta$.

We use the observations and analysis of the most recent analysis cycle, which will be published as the fourth GALAH data release ([Buder et al. 2024](#)). The spectra are reduced using a similar analysis as that for the third data release ([Buder et al. 2021](#)), with a custom-built reduction pipeline ([Kos et al. 2017](#)). Stellar parameters—that is, effective temperature (T_{eff}), surface gravity ($\log g$), and radial, microturbulence, and rotational velocities (v_{rad} , v_{mic} and $v \sin i$), as well as up to 31 elemental abundances—are then simultaneously estimated by minimizing the weighted residuals between the

³ <https://github.com/acbecker/hotpants>

⁴ <https://gsaweb.ast.cam.ac.uk/alerts/alert/Gaia22ahy/>

observed and synthetic stellar spectra. The latter are interpolated with a high-dimensional neural network (compare to [Ting et al. 2019](#)), trained on synthetic stellar spectra generated with the spectrum synthesis code Spectroscopy Made Easy ([Piskunov & Valenti 2017](#)), and degraded to the measured instrumental resolution of the spectrum. This change with respect to the third data release, which used wavelength regions of carefully selected unblended lines, allows 94% of the observed wavelength range to be used and thus considerably increases the measurement precision.

The spectroscopic fit also includes photometric and astrometric information from the 2MASS ([Skrutskie et al. 2006](#)) and Gaia surveys ([Lindgren et al. 2021a](#)) to constrain the surface gravity. This leads to more accurate stellar parameters, as shown in the previous HERMES analyses ([Buder et al. 2018, 2019, 2021](#)), particularly for cool giant stars such as the target of this study, where molecular features complicate the spectroscopic analysis. The fit is very good, with the signal-to-noise ratio increasing across the four wavelength regions (16, 107, 194, and 254), as can be seen from Figure 2. We do not expect a good fit to the Balmer-line cores or the lithium lines at 4861, 6563, and 6708 Å, respectively. No quality concerns are raised by the automatic pipeline (`flag_sp` = 0).

The final radial velocity of $v_{\text{rad}} = -72.44 \pm 0.18 \text{ km s}^{-1}$ is in very good agreement with the value from the Gaia DR3 spectrum—that is, $v_{\text{rad,Gaia}} = -71.8 \pm 1.0 \text{ km s}^{-1}$ ([Recio-Blanco et al. 2023](#)). The final stellar parameters are $T_{\text{eff}} = 3776 \pm 67 \text{ K}$, $\log g = 1.05 \pm 0.12$, $[\text{Fe}/\text{H}] = -0.148 \pm 0.053$, $v_{\text{mic}} = 1.82 \pm 0.28 \text{ km s}^{-1}$, and $v \sin i = 5.5 \pm 1.4 \text{ km s}^{-1}$. The stellar abundances are close to the solar values; for example, $[\text{Mg}/\text{Fe}] = 0.007 \pm 0.011$.

3. LIGHT-CURVE ANALYSIS

3.1. *Single-lens Model*

In a microlensing event, the flux is modeled as

$$f(t) = f_{\text{S}} \cdot A(t) + f_{\text{B}}, \quad (4)$$

where $A(t)$ is the magnification as a function of time, and f_{S} and f_{B} are the source flux and the blended flux within the PSF, respectively. In the simplest single-lens single-source (1L1S) model, i.e., the PSPL model ([Paczynski 1986](#)), the magnification is given by

$$A_{\text{PSPL}} = \frac{u^2 + 2}{u\sqrt{u^2 + 4}}; \quad u(t) = \sqrt{u_0^2 + \frac{(t - t_0)^2}{t_{\text{E}}^2}}, \quad (5)$$

where u is the angular lens-source separation normalized by θ_{E} , and (t_0, u_0) are the time of the closest source-lens approach and the impact parameter normalized by θ_{E} , respectively.

The peak of the light curve (Figure 1) is flattened compared to the PSPL model, suggesting possible finite-source effects ([Gould 1994a](#)). We fit the FSPL model to the light curve by introducing an additional parameter, $\rho = \theta_*/\theta_{\text{E}}$. In the FSPL model, A_{FSPL} is calculated by integrating A_{PSPL} over a limb-darkened source disk. Using the best-fit spectroscopic parameters (see § 2.3), we estimate the limb-darkening coefficients $(\Gamma_{g'}, \Gamma_{r'}, \Gamma_{i'}, \Gamma_G, \Gamma_K) = (0.91, 0.77, 0.63, 0.74, 0.29)$ based on [Claret & Bloemen \(2011\)](#) and [Claret \(2019\)](#).

The best-fit FSPL model is shown as a dashed black line in the top panel of Figure 1, and the residuals are shown in the bottom panel. The residuals exhibit significant trends deviating from the

FSPL model, spanning ~ 10 days around the peak (at $\text{HJD}' \sim 9600$). These systematic deviations cannot be absorbed by adjusting either the limb-darkening coefficients or the free parameters in the FSPL models. Deviations from single-lens models suggest the possible existence of a companion to the lens or the source. There is also a ~ 0.1 mag broad bump-like feature in the Gaia G -band light curve at around ~ 300 days before the peak (see the right panel of Figure 3). Such an additional feature excludes single-lens binary-source models, and we study binary-lens models in the following.

3.2. Binary-lens Model

The light curve can be well described by the binary-lens single-source (2L1S) model. We start the analysis with the static binary-lens model, which includes three additional parameters (s, q, α) to describe a nonrotating binary-lens system: s is the projected angular separation of the binary components normalized by θ_E , q is the binary mass ratio, and α is the angle between the source-lens trajectory and the binary-lens axis. We use the advanced contour integration package **VBBinaryLensing** (Bozza 2010; Bozza et al. 2018) to calculate the binary-lens magnification $A(t, \Theta_{2\text{L1S}})$, given the parameters $\Theta_{2\text{L1S}} = \{s, q, \alpha, \rho, t_0, u_0, t_E\}$.

We start by scanning the seven-dimensional parameter space on a fixed $(\log s, \log q, \alpha)$ grid with $-1 \leq \log s \leq 1$, $-2 \leq \log q \leq 1$ and $0 \leq \alpha < 2\pi$. At each grid point, we minimize the χ^2 by setting the four remaining parameters ($t_0, u_0, t_{\text{eff}} \equiv u_0 t_E, t_* \equiv \rho t_E$) free in Markov Chain Monte Carlo (MCMC) using the **EMCEE** package (Foreman-Mackey et al. 2013). The resulting χ^2 map is shown in Figure 4, from which we identify five local minima in the close-binary ($s < 1$) regime and nine local minima in the wide-binary ($s > 1$) regime. The severe finite-source effects smear out the sharp magnification structure of caustics, leading to a plethora of local minima over a broad range of $\log q$. For close solutions, there is a perfect degeneracy of $(\log q, \alpha) \rightarrow (-\log q, \alpha + \pi)$, and therefore we only conduct the grid search with $\log q \leq 0$. For wide solutions, we have a fourfold degeneracy in α . When $q \gg 1$, the “planetary” caustic associated with secondary mass is reduced to a Chang-Refsdal (Chang & Refsdal 1979) caustic with shear $s^{-2}/q \ll 1$. The four identical cusps of Chang-Refsdal lead to a degeneracy of $\alpha \rightarrow \alpha + \pi/2$, as shown in Figure 4. The solutions with $q \gg 1$ can correspond to an unrealistic value of t_E . We limit our analysis to $\log q < 3$, which corresponds to an upper limit of $t_E \sim 2000$ days.

Then we probe all local minima by setting all the parameters free in MCMC. We also introduce higher-order effects into the modeling. We include the annual microlens parallax effects (Gould 1992), which are the light-curve distortions due to the Earth’s orbital acceleration toward the Sun. The static binary-lens model has a perfect geometric degeneracy $(u_0, \alpha) \rightarrow -(u_0, \alpha)$, which is broken when taking the microlens parallax into account. For the $u_0 > 0$ and $u_0 < 0$ geometry, the lens takes different sides of the source trajectory, leading to different magnifications. As defined in Gould (2004), the microlens parallax vector $\boldsymbol{\pi}_E$ is described by the east and north components $\boldsymbol{\pi}_E = (\pi_{E,E}, \pi_{E,N})$. We also consider the orbital motion of the binary lens, which can have degeneracies with microlens parallax (Batista et al. 2011; Skowron et al. 2011). We apply the linearized orbital motion

$$s(t) = s_0 + \frac{ds}{dt}(t - t_0); \quad \alpha(t) = \alpha_0 + \frac{d\alpha}{dt}(t - t_0). \quad (6)$$

with the two parameters ds/dt and $d\alpha/dt$. This approximation is subject to physical constraints, as discussed in Dong et al. (2009). For a bound system, the ratio of the projected kinetic to the

potential energy β should be less than unity:

$$\beta = \left| \frac{\text{KE}_\perp}{\text{PE}_\perp} \right| = \frac{(\gamma \cdot \text{yr})^2}{8\pi^2} \frac{M_\odot \kappa \pi_E}{\theta_E} \left(\frac{s}{\pi_E + \pi_S/\theta_E} \right)^3 < 1, \quad (7)$$

where $\gamma = (ds/s dt, d\alpha/dt)$ and π_S is the trigonometric parallax of the source star. We adopt $\theta_E = 0.73 \text{ mas}$ and $\pi_S = 0.185 \text{ mas}$ (see § 5.1) and restrict the MCMC exploration to $\beta < 1$.

We find that the best-fit solution is a wide binary with $u_0 < 0$ and we label it as “wide A–”. The source trajectory and caustics are shown in the upper left subpanel of Figure 3. The “wide A–” solution has $\chi^2 = 948.9$, and all other solutions are worse by $\Delta\chi^2 > 50$. Nevertheless, we keep all solutions with $\Delta\chi^2 < 81$ (listed in Table 1) for further analysis incorporating the VLTI GRAVITY data.

4. INTERFEROMETRIC DATA ANALYSIS

4.1. Parameterization

The images generated from the binary-lens equation are oriented with respect to the binary-lens axis and in the units of the Einstein radius, so they need to be rotated to the sky plane and scaled by θ_E to compute the closure phases. We define Ψ as the position angle of the binary-lens axis. The direction of the lens-source relative motion $\boldsymbol{\mu}_{\text{rel}}$, which is the same as that of the microlens parallax $\boldsymbol{\pi}_E$, can be expressed as

$$\Phi_\pi = \alpha + \Psi \quad (8)$$

We incorporate the two parameters $\{\theta_E, \Psi\}$ in addition to the 2L1S parameters $\{s, q, \alpha, \rho, t_0, u_0, t_E\}$ for modeling the interferometric data. The microlens parallax is reparameterized by $(\pi_{E,N}, \pi_{E,E}) = \pi_E \cdot (\cos \Phi_\pi, \sin \Phi_\pi)$ with $\Phi_\pi = \alpha + \Psi$.

4.2. Probing Interferometric Observables

Prior to carrying out the full joint analysis of VLTI and light curve, we first investigate the VLTI parameters with limited input from the light-curve models. We start the investigation using only (s, q, ρ) from the best-fit light-curve model “wide A–.” We perform a four-dimensional grid search on $(\theta_E, \Psi, u_x, u_y)$ to fit the closure-phase data from each of the eight VLTI exposures, where (u_x, u_y) are the source’s coordinates on the binary-lens plane. At each grid point, we generate the images scaled and rotated to the sky plane based on (θ_E, Ψ) and then calculate the closure phases and corresponding $\chi_{\text{VLTI},i}^2(\theta_E, \Psi, u_x, u_y)$ for every VLTI exposure i . We describe our method of calculating the closure phase from the binary-lens images in Appendix B. Our closure-phase calculations from the images are validated with the PMOIRE software⁵ (Mérand 2022).

To exclude unreasonable source positions, we add a penalty term,

$$\chi_i^2 = \chi_{\text{VLTI},i}^2 + \left(\frac{A(u_{x,i}, u_{y,i}) - A_{\text{LC},i}}{0.1 A_{\text{LC},i}} \right)^2, \quad (9)$$

for the deviation from light-curve magnification for each VLTI exposure i , where $A_{\text{LC},i}$ is the magnification from the “wide A–” model at the i th VLTI exposure, and we adopt a fractional error of 10% so that $(u_{x,i}, u_{y,i})$ are only subject to loose light-curve magnification constraints.

⁵ <https://github.com/amerand/PMOIRE>

A self-consistent VLTI model should have the same values of (θ_E, Ψ) on all the exposures. Therefore, for each set of (θ_E, Ψ) , we calculate

$$\chi_{\text{tot}}^2(\theta_E, \Psi) = \sum_i \min [\chi_i^2(\theta_E, \Psi, u_{x,i}, u_{y,i})], \quad (10)$$

where $\min [\chi_i^2(\theta_E, \Psi, u_{x,i}, u_{y,i})]$ is the minimum χ^2 for a given (θ_E, Ψ) in the i -th VLTI exposure.

The left panel of Figure 5 shows the $\Delta\chi_{\text{tot}}^2(\theta_E, \Psi)$ map, from which we identify four local minima. The θ_E is within a broad range of $0.6 - 1.0$ mas, and Ψ is subject to a fourfold degeneracy around $(-100^\circ, -10^\circ, 80^\circ, 170^\circ)$, each with an uncertainty of $\sim 10^\circ$. The fourfold degeneracy corresponds to having the source positions near the four cusps of the “central” caustic associated with the primary mass, resulting in similar image morphologies that are compatible with the VLTI data (see the subpanels on the right of Figure 5).

Next, we further probe the four local minima by jointly fitting all epochs of VLTI data. In a satisfactory VLTI microlensing model, the source positions should lie approximately on a straight line, following the source-lens relative motion, so we parameterize the source positions (u_x, u_y) with (u_0, t_0, t_E, α) as

$$\begin{aligned} u_x &= u_0 \sin \alpha - \tau \cos \alpha, \\ u_y &= -u_0 \cos \alpha - \tau \sin \alpha, \end{aligned}$$

where $\tau = (t - t_0)/t_E$. The interferometric parameters (θ_E, Ψ) are seeded from the abovementioned four local minima. We allow $(\log s, \log q, \log \rho)$ to freely vary, and we no longer add the χ^2 penalty term as in Eq. 9. The four best-fit solutions have similar χ^2 ($\Delta\chi^2 < 10$), so the VLTI data alone cannot distinguish between them. All the solutions strongly prefer $u_0 < 0$. As in the previous single-lens events, $u_0 > 0$ and $u_0 < 0$ solutions can be distinguished with two or more epochs of VLTI data (Dong et al. 2019; Zang et al. 2020; Cassan et al. 2022). The four degenerate solutions correspond to four distinct α values, denoted as α_{VLTI} , which are displayed as the shaded regions in Figure 6. The allowed $(\log s, \log q)$ from the posteriors have broad ranges, suggesting that the resulting constraints on α_{VLTI} are not specific to the seed solution of “wide A–,” so we use them as the starting point for the joint analysis with the light curves in § 4.3.

4.3. Joint Analysis with Light Curves

In this section, we present the joint analysis of VLTI and light-curve modeling. We begin by comparing the light-curve parameters and VLTI constraints. Figure 6 shows the comparisons between the α parameters α_{LC} derived from the light-curve solutions with α_{VLTI} . The three solutions are mutually compatible within 3σ , and they are all at $\Psi \sim -100^\circ$. These include one close solution (“close A–”) and two wide solutions (“wide A–” and “wide B+”). Next we check the consistency of the direction π_E between the light-curve solutions and VLTI solution at $\Psi \sim -100^\circ$. Figure 7 displays the posterior distribution of $(\pi_{E,E}, \pi_{E,N})$ and the Φ_π constraint from VLTI. For three light-curve solutions (“wide A–”, “wide B+”, and “close A–”), the two directions agree to $\sim 1\sigma$.

Then we perform a joint fit to the VLTI and light-curve data for the “wide A–”, “wide B+”, and “close A–” solutions. We include the higher-order effects of the microlens parallax and binary orbital motion. In addition, we account for the limb-darkening effects in the closure-phase modeling by adopting $\Gamma_K = 0.29$, based on our adopted source stellar parameters (§ 3.1). Compared to

the uniform-brightness profile, limb darkening presents minor improvements in the goodness of fit, with $\Delta\chi^2 \sim (3, 7, 8)$ for the solutions (wide A−, wide B+, close A−), respectively, and the best-fit parameters with and without the limb-darkening effects are consistent with each other. Thus, the non-limb-darkening approximation adopted in the closure-phase analysis is adequate for probing local minima with grid searches (§ 4.2). Nevertheless, we consider the limb-darkening effects to derive the final results from the joint fit.

Table 2 lists the best-fit parameters and their uncertainties. The global best fit is the “wide A−” solution, and Figure 8 shows its best-fit closure-phase models along with the geometric configurations of the source, caustic, and images. The “close A−” solution is worse by $\Delta\chi^2 \approx 45$, which is somewhat (≈ 25) less compared with the light-curve-only $\Delta\chi^2$. Therefore, the preference for the “wide A−” over the “close A−” comes from the light-curve fitting. It mainly stems from the ~ 0.1 mag broad bump around $\text{HJD}' \sim 9300$ in the Gaia light curve, as mentioned in § 3.1. This feature can be well matched by the wide solutions. In contrast, for the “close A−” solutions, the orbital motion parameters can be tuned to induce source crossing of a planetary caustic at $\text{HJD}' \sim 9300$, but the corresponding perturbation is too sharply peaked to reproduce the observed broad feature (see the right panel of Figure 3). Among the wide solutions, the “wide B+” model fit is worse by $\Delta\chi^2 \approx 296$ with respect to “wide A−,” significantly increased by ≈ 245 compared with light curve only. As discussed in § 4.2, such $u_0 > 0$ geometries are strongly disfavored by the constraints from multi-epoch VLTI data.

To further understand the VLTI constraints on these three solutions, we performed additional fitting with the interferometric data only. We hold the parameters $(s, q, \rho, \Psi, \theta_E)$, which define the caustics’ configuration, fixed at their best-fit values from the joint modeling, while the source positions (u_x, u_y) of the three nights are allowed to vary. Figure 9 shows the 3σ (u_x, u_y) contours (magenta) compared with the expected source positions (black dots) on the best-fit trajectory (black solid line) from the joint modeling for each solution. For the “wide A−” solution, there is a $\gtrsim 3\sigma$ discrepancy in (u_x, u_y) during Night 1, which corresponds to the $\lesssim 0.3^\circ$ systematic residuals of the closure phases for U4U2U1 and U4U3U2 in both exposures of that night, as displayed in the top two subpanels of Figure 8. During the other two nights, the source positions are in good agreement with the “wide A−” solution. Note that such $\sim 0.3^\circ$ systematic offsets also show up in the third exposure of Night 2 (see Figure 8), but they are not present in the other three exposures (i.e., Night 2-1, 2-2, and 2-4), which are in good agreement with the model. This suggests the existence of sub-degree-level systematic error in the closure-phase data. The “close A−” solution shows a similar degree of consistency to the “wide A−.” In contrast, for the “wide B+” solution, which is ruled out by the VLTI data, the source positions of all three nights deviate by $> 3\sigma$ from the expectation.

In conclusion, because the “wide A−” solution is preferred over all other local minima by $\Delta\chi^2 \gtrsim 45$, we regard it as the only favored solution of ASASSN-22av.

5. PHYSICAL PARAMETERS

5.1. Source Properties and Finite-source Effects

The finite-source effects exhibited in ASASSN-22av’s light curves provide an opportunity to cross-check the VLTI-measured θ_E with $\theta_E = \theta_*/\rho$. The standard method (Yoo et al. 2004) for deriving θ_* for bulge microlensing events uses the source’s dereddened color and magnitude with the extinction coefficients estimated from the location of bulge red clump (RC) stars in a color-magnitude diagram (CMD). In our case, the source star is not toward the bulge, and the CMD contains RC stars

at a variety of distances, making it difficult to apply the standard method. Gaia DR3 reports a trigonometric parallax $\pi_S = 0.137 \pm 0.016$ mas. We adopt $\pi_{S,\text{corr}} = 0.185$ mas after applying the preliminary zero-point correction from Lindegren et al. (2021b). The independent investigation on the Gaia parallax zero-point offset by Groenewegen (2021) yields a consistent value of $\pi_{S,\text{corr}} = 0.207 \pm 0.025$ mas. We fit the spectral energy distribution (SED) using photometric data from 2MASS, Gaia and SkyMapper Southern Survey DR4 (Onken et al. 2024). We employ the MESA Isochrones and Stellar Tracks (MIST; Choi et al. 2016) to generate synthetic magnitudes as a function of stellar mass, age, and metallicity. The extinction $E(B - V)$ is taken as a free parameter with a flat prior, and we assume that $R_V = 3.1$. We use the corrected Gaia parallax as a prior for source distance. MIST returns the stellar radius R_* , and hence the angular radius $\theta_* = R_*/D_S$ can be estimated with MCMC. The photometric error bars are inflated by a factor of 2, so that $\chi^2/\text{dof} \sim 1$. We find that the best-fit $E(B - V) = 0.64^{+0.06}_{-0.04}$, which is consistent with the lower limit of $E(B - V) > 0.61$ (for distance greater than 4.3 kpc), according to the three-dimensional dust map of Guo et al. (2021). The best-fit stellar parameters are $T_{\text{eff}} = 3747^{+46}_{-18}$ K, $\log g = 1.07^{+0.11}_{-0.04}$ and $[\text{Fe}/\text{H}] = 0.01^{+0.12}_{-0.07}$, arriving at $\theta_* = 44.0 \pm 0.8 \mu\text{as}$. The SED-derived stellar parameters are consistent with the spectroscopic ones from § 2.3.

For the best-fit “wide A−” solution with $\rho = 0.058 \pm 0.001$, we find $\theta_E = 0.759 \pm 0.019$ mas, which differs by 1.8σ from the $\theta_E = 0.724 \pm 0.002$ mas determined by VLTI GRAVITY. In comparison, for the “close A−” solution, where $\rho = 0.051^{+0.001}_{-0.001}$, the corresponding $\theta_E = 0.862 \pm 0.023$ mas deviates from the VLTI GRAVITY value of $\theta_E \simeq 0.737 \pm 0.002$ mas by 5.4σ . Note that the $\sim 2\%$ error of our θ_* estimate is likely an underestimate, due to unaccounted-for systematic uncertainties. For example, θ_* inferences from the empirical color/surface brightness relations such as Kervella et al. (2004) generally have errors of $\sim 4\%$ – 5% . In any case, for the “wide A−” solution, θ_E derived from VLTI and finite-source effects are basically consistent.

5.2. Physical Properties of the Lens System

With measurements of the angular Einstein radius θ_E and the microlens parallax π_E , the physical parameters of the lens system can be unambiguously derived from microlensing observables:

$$M_L = \frac{\theta_E}{\kappa \pi_E}; \quad \pi_{\text{rel}} = \theta_E \pi_E; \quad \mu_{\text{rel}} = \frac{\theta_E}{t_E} \frac{\pi_E}{\pi_E}, \quad (11)$$

and adopting $\pi_S = 0.185 \pm 0.016$ mas, we can also infer the lens distance:

$$D_L = \frac{\text{au}}{\pi_E \theta_E + \pi_S}. \quad (12)$$

The lens properties of the favored solution (“wide A−”) are listed in Table 3. The lens system is composed of two M dwarfs with $M_1 = 0.256^{+0.008}_{-0.006} M_\odot$ and $M_2 = 0.130 \pm 0.007 M_\odot$, separated by a projected separation of $r_\perp = 6.83 \pm 0.31$ au and at a distance of $D_L = 2.29 \pm 0.08$ kpc.

Based on MIST isochrones, we estimate that the lens system has $K_s = 18.5$ (assuming zero extinction). In comparison, the source’s 2MASS magnitude is $K_s = 9.27$. During the VLTI observations, the magnification is more than 15, and thus the flux ratio between the lens and magnified source is $\xi = f_L/(Af_S) < 1.4 \times 10^{-5}$. Therefore, the lens light has a negligible effect on the closure phase, justifying our approach of calculating closure phases without the lens flux contribution.

6. DISCUSSION AND CONCLUSION

ASASSN-22av is the first binary-lens microlensing event with multiple images resolved by interferometry. The modeling is considerably more complex than for a single-lens event. For a typical single-lens event, the simple model of two point images is generally satisfactory for fitting the closure-phase data (Dong et al. 2019), and thus closure-phase modeling can, in principle, be performed separately from the light curve. In contrast, a binary lens has three or five images for a point source, depending on whether the source is outside or inside the caustics. During the VLTI observations of ASASSN-22av, the images, formed from a finite source crossing caustics, morphed from a nearly complete Einstein ring to separated arcs over a period of several nights. Thus, the interpretation of the closure-phase data from such a binary-lens event requires inputs from light-curve modeling.

The weak binary-lens perturbation and sparse pre-peak photometric coverage make the light-curve modeling particularly complicated for ASASSN-22av. In the early stages of our work, where we did not include the Gaia light curve, we found 25 local minima in our binary-lens grid search. After incorporating the VLTI data, the best-fit solution, which is the same as the presently favored “wide A–” solution, ‘predicted’ the existence of the bump at $\text{HJD}' \sim 9300$ shown in the Gaia light curve. We only realized this ‘prediction’ later, after conducting light-curve modeling after the inclusion of Gaia data. The predictive power of the “wide A–” solution offers good evidence for its validity.

We also made several consistency checks between the light curve and multi-epoch VLTI data. For the favored solution, there are good agreements in multiple aspects, including α (Figure 6), direction of π_E (Figure 7), source trajectory (Figure 9), and θ_E (see the discussion in § 5.1), further demonstrating the model’s robustness. The agreement between the best-fit model and the closure-phase data is at $\lesssim 0.3^\circ$ (Figure 8, §4.3), which likely reflects the instrument’s systematics floor. We measure the Einstein radius $\theta_E = 0.724 \text{ mas}$ with 0.3% precision, even though it is close to the smallest value resolvable by VLTI GRAVITY. The expected closure phase would be $\lesssim 5^\circ$ for θ_E to 0.6 mas and $\lesssim 2^\circ$ for $\theta_E = 0.5 \text{ mas}$.

The lens system consists of two M dwarfs separated by $\sim 6.8 \text{ au}$ at 2.3 kpc, with $(M_1, M_2) = (0.256 \pm 0.008, 0.130 \pm 0.007) M_\odot$. The primary mass is more precisely determined than the secondary (3.1% versus 5.4%). This is because, in the wide-binary ($s > 1$) regime, the scale of images (measured by VLTI GRAVITY) is proportional to θ_E of the primary mass rather than the total mass. Hence, the uncertainty of the secondary mass M_2 is contributed by an additional uncertainty from the mass ratio. The estimated orbital period is $P \sim 28 \text{ yr}$ for a circular orbit, and the angular separation between the binaries is $\sim 3 \text{ mas}$ at 2.3 kpc. Such faint low-mass binary systems at intermediate orbital separations have so far been inaccessible by any other method (see, e.g., Figure 1 of El-Badry 2024). Similar VLTI microlensing observations will be able to identify and characterize intermediate binaries containing dark compact objects like neutron stars and stellar-mass black holes to complement other detection techniques.

ACKNOWLEDGMENT

We thank Cheongho Han and Gregory Green for helpful discussions. This work is based on observations collected at the European Southern Observatory under Director Discretionary Time program 108.23MK. This work is supported by the National Natural Science Foundation of China (grant No. 12133005) and the science research grants from the China Manned Space Project with No. CMS-CSST-2021-B12. S.D. acknowledges the New Cornerstone Science Foundation through the

XPLORER PRIZE. C.S.K. is supported by NSF grants AST-2307385 and 2407206. This research was funded in part by the National Science Centre, Poland, and grants OPUS 2021/41/B/ST9/00252 and SONATA 2023/51/D/ST9/00187 awarded to P.M.

This research uses data obtained through the Telescope Access Program (TAP), which has been funded by the TAP member institutes. This work has made use of data from the European Space Agency (ESA) mission Gaia (<https://www.cosmos.esa.int/gaia>), processed by the Gaia Data Processing and Analysis Consortium (DPAC; <https://www.cosmos.esa.int/web/gaia/dpac/consortium>). Funding for the DPAC has been provided by national institutions, in particular the institutions participating in the Gaia Multilateral Agreement. We acknowledge the Gaia Photometric Science Alerts Team. We also acknowledge the devoted staff of the Anglo-Australian Telescope who have maintained the HERMES spectrograph over a decade.

This research has made use of the VizieR catalog access tool, CDS, Strasbourg, France. This publication makes use of data products from the Two Micron All Sky Survey, which is a joint project of the University of Massachusetts and the Infrared Processing and Analysis Center/California Institute of Technology, funded by the National Aeronautics and Space Administration and the National Science Foundation.

APPENDIX

A. BINNING THE CLOSURE-PHASE DATA

The interferometric observables are the complex visibilities \mathcal{V}_{pq} and closure phases ϕ_{pqr} , with (van Cittert 1934; Zernike 1938)

$$\mathcal{V}_{pq}(u, v; \lambda) = \frac{\int I(\alpha, \delta) e^{-2\pi i(u\alpha + v\delta)} d\alpha d\delta}{\int I(\alpha, \delta) d\alpha d\delta}, \quad (\text{A1})$$

where $I(\alpha, \delta)$ is the on-sky target intensity distribution centered on the light of sight (α_0, δ_0) and $(u, v) = (\mathbf{n}_E, \mathbf{n}_N) \cdot \mathbf{B}_{pq}/\lambda$ is the on-sky projection of the baseline vector over wavelength. The closure phase is defined for a three-telescope array as $\phi_{pqr}(\lambda) = \arg(\mathcal{V}_{pq}\mathcal{V}_{qr}\mathcal{V}_{rp})$. For a list of closure phases $\{\phi_k\}$, the mean closure phase $\bar{\phi}$ is calculated by assigning ϕ_k to the unit complex and summing them up for binning as

$$\bar{\phi} = \arg \sum_k e^{i\phi_k}. \quad (\text{A2})$$

The uncertainty of $\bar{\phi}$ is estimated using bootstrap resampling.

B. IMAGE GENERATION AND VISIBILITY CALCULATION

For a given set of source coordinate (u_x, u_y) and binary configuration (s, q) , we extract the image contours used for the magnification calculation in `VBBinaryLensing` package. The contours are then converted to two-dimensional images using the loop-linking method (Dong et al. 2006), which combines the contour integration and inverse-ray-shooting methods. The loop-linking method fills the contour with a uniform grid of points organized in links. At a given step size δ , our code returns the head (x_k, y_k) and the number of points n_k of the k th link, which contains a set of points $(x_k, y_k + j\delta)$ with $j \in \{0, 1, 2, \dots, n_k - 1\}$. For any baseline coordinate (u, v) , the complex visibility is calculated

by summing up the contribution from all links (assuming $\Psi = 0$) as

$$\begin{aligned}\mathcal{V}(u, v) &= \sum_k \sum_{j=0}^{n_k-1} e^{-2\pi i(vx_k + u(y_k + j\delta))} \\ &= \sum_k e^{-2\pi i(vx_k + uy_k)} \sum_{j=0}^{n_k-1} (e^{-2\pi iu\delta})^j \\ &= \sum_k e^{-2\pi i(vx_k + uy_k)} \frac{1 - e^{-2\pi iu\delta n_k}}{1 - e^{-2\pi iu\delta}}.\end{aligned}$$

The calculation is optimized by grouping the links by n_k and summing up them first, which reduces the number of calculations by a factor of ~ 2 . We caution that the dot product of (x_k, y_k) and (u, v) is not arbitrary. In our case, it has to be $x_kv + y_ku$. Otherwise, the transformation from the image plane to the sky plane is not positive-definite and the angle Ψ is not well-defined.

An alternative method for computing the visibility is applying the divergence theorem on the closed image contour ∂D with

$$V(\mathbf{u}) = \iint_D e^{-2\pi i\mathbf{u}\cdot\mathbf{r}} d^2\mathbf{r} = \oint_{\partial D} e^{-2\pi i\mathbf{u}\cdot\mathbf{r}} \frac{\mathbf{u} \cdot \hat{\mathbf{n}}}{-2\pi iu^2} ds, \quad (\text{B3})$$

where $\hat{\mathbf{n}}$ is the unit vector normal to the boundary ∂D at \mathbf{r} . For a closed polygon with vertices \mathbf{r}_k , the integration for edge $\mathbf{r}_k \rightarrow \mathbf{r}_{k+1}$ is

$$\int_{\mathbf{r}_k}^{\mathbf{r}_{k+1}} e^{-2\pi i\mathbf{u}\cdot\mathbf{r}} \frac{\mathbf{u} \times d\mathbf{r}}{-2\pi iu^2} = \frac{1}{4\pi^2 u^2} \frac{\mathbf{u} \times (\mathbf{r}_k - \mathbf{r}_{k+1})}{\mathbf{u} \cdot (\mathbf{r}_k - \mathbf{r}_{k+1})} (e^{-2\pi i\mathbf{u}\cdot\mathbf{r}_k} - e^{-2\pi i\mathbf{u}\cdot\mathbf{r}_{k+1}}). \quad (\text{B4})$$

The visibility is then the sum over all edges. This method is faster than the loop-linking method for convex images, while the loop-linking method is faster for concave images. In our case, the images are ring-like arcs, and thus we adopt the loop-linking method.

Software: PmPyeasy, hotpants, DoPHOT, VBBinaryLensing, EMCEE, PMOIRE, MIST

REFERENCES

- | | |
|---|--|
| <p>Afonso, C., Albert, J. N., Andersen, J., et al. 2001, A&A, 378, 1014.
doi:10.1051/0004-6361:20011204</p> <p>Alard, C. & Lupton, R. H. 1998, ApJ, 503, 325.
doi:10.1086/305984</p> <p>Alard, C. 2000, A&AS, 144, 363.
doi:10.1051/aas:2000214</p> <p>Albrow, M., An, J., Beaulieu, J.-P., et al. 2001, ApJL, 550, L173. doi:10.1086/319635</p> <p>An, J. H., Albrow, M. D., Beaulieu, J.-P., et al. 2002, ApJ, 572, 521. doi:10.1086/340191</p> | <p>Batista, V., Gould, A., Dieters, S., et al. 2011, A&A, 529, A102.
doi:10.1051/0004-6361/201016111</p> <p>Becker, A. 2015, Astrophysics Source Code Library. ascl:1504.004</p> <p>Bernstein, R., Sheiman, S. A., Gunnels, S. M., et al. 2003, Proc. SPIE, 4841, 1694.
doi:10.1117/12.461502</p> <p>Bozza, V. 2010, MNRAS, 408, 2188.
doi:10.1111/j.1365-2966.2010.17265.x</p> <p>Bozza, V., Bachelet, E., Bartolić, F., et al. 2018, MNRAS, 479, 5157. doi:10.1093/mnras/sty1791</p> |
|---|--|

- Brown, T. M., Baliber, N., Bianco, F. B., et al. 2013, *PASP*, 125, 1031. doi:10.1086/673168
- Buckley, D. A. H., Swart, G. P., & Meiring, J. G. 2006, *Proc. SPIE*, 6267, 62670Z. doi:10.1117/12.673750
- Buder, S., Asplund, M., Duong, L., et al. 2018, *MNRAS*, 478, 4513. doi:10.1093/mnras/sty1281
- Buder, S., Lind, K., Ness, M. K., et al. 2019, *A&A*, 624, A19. doi:10.1051/0004-6361/201833218
- Buder, S., Sharma, S., Kos, J., et al. 2021, *MNRAS*, 506, 150. doi:10.1093/mnras/stab1242
- Buder, S., Kos, J., Wang, E. X., et al. 2024, arXiv:2409.19858. doi:10.48550/arXiv.2409.19858
- Cassan, A., & Ranc, C. 2016, *MNRAS*, 458, 2074
- Cassan, A., Ranc, C., Absil, O., et al. 2022, *Nature Astronomy*, 6, 121. doi:10.1038/s41550-021-01514-w
- Chang, K. & Refsdal, S. 1979, *Nature*, 282, 561. doi:10.1038/282561a0
- Chen, P., Dong, S., Kochanek, C. S., et al. 2022, *ApJS*, 259, 53. doi:10.3847/1538-4365/ac50b7
- Choi, J., Dotter, A., Conroy, C., et al. 2016, *ApJ*, 823, 102. doi:10.3847/0004-637X/823/2/102
- Claret, A. & Bloemen, S. 2011, *A&A*, 529, A75. doi:10.1051/0004-6361/201116451
- Claret, A. 2019, *VizieR Online Data Catalog*, 6154. VI/154
- Dalal, N., & Lane, B. F. 2003, *ApJ*, 589, 199
- Delplancke, F., Górski, K. M., & Richichi, A. 2001, *A&A*, 375, 701
- De Silva, G. M., Freeman, K. C., Bland-Hawthorn, J., et al. 2015, *MNRAS*, 449, 2604. doi:10.1093/mnras/stv327
- Dong, S., DePoy, D. L., Gaudi, B. S., et al. 2006, *ApJ*, 642, 842. doi:10.1086/501224
- Dong, S., Udalski, A., Gould, A., et al. 2007, *ApJ*, 664, 862. doi:10.1086/518536
- Dong, S., Gould, A., Udalski, A., et al. 2009, *ApJ*, 695, 970. doi:10.1088/0004-637X/695/2/970
- Dong, S., Mérand, A., Delplancke-Ströbele, F., et al. 2019, *ApJ*, 871, 70. doi:10.3847/1538-4357/aaeffb
- Einstein, A. 1936, *Science*, 84, 506. doi:10.1126/science.84.2188.506
- Eisenhauer, F., Monnier, J. D., & Pfuhl, O. 2023, *ARA&A*, 61, 237. doi:10.1146/annurev-astro-121622-045019
- El-Badry, K. 2024, *NewAR*, 98, 101694. doi:10.1016/j.newar.2024.101694
- Foreman-Mackey, D., Hogg, D. W., Lang, D., et al. 2013, *PASP*, 125, 306. doi:10.1086/670067
- Gaia Collaboration, Prusti, T., de Bruijne, J. H. J., et al. 2016, *A&A*, 595, A1. doi:10.1051/0004-6361/201629272
- Gaia Collaboration, Vallenari, A., Brown, A. G. A., et al. 2023, *A&A*, 674, A1. doi:10.1051/0004-6361/202243940
- Gould, A. 1992, *ApJ*, 392, 442. doi:10.1086/171443
- Gould, A. 1994, *ApJL*, 421, L71. doi:10.1086/187190
- Gould, A. 1994, *ApJL*, 421, L75. doi:10.1086/187191
- Gould, A., Miralda-Escude, J., & Bahcall, J. N. 1994, *ApJL*, 423, L105. doi:10.1086/187247
- Gould, A. 2000, *ApJ*, 542, 785
- Gould, A. 2004, *ApJ*, 606, 319. doi:10.1086/382782
- GRAVITY Collaboration, Abuter, R., Accardo, M., et al. 2017, *A&A*, 602, A94. doi:10.1051/0004-6361/201730838
- GRAVITY+ Collaboration, Abuter, R., Allouche, F., et al. 2022a, *A&A*, 665, A75. doi:10.1051/0004-6361/202243941
- GRAVITY+ Collaboration, Abuter, R., Alarcon, P., et al. 2022b, *The Messenger*, 189, 17. doi:10.18727/0722-6691/5285
- Groenewegen, M. A. T. 2021, *A&A*, 654, A20. doi:10.1051/0004-6361/202140862
- Guo, H.-L., Chen, B.-Q., Yuan, H.-B., et al. 2021, *ApJ*, 906, 47. doi:10.3847/1538-4357/abc68a
- Hodgkin, S. T., Harrison, D. L., Breedt, E., et al. 2021, *A&A*, 652, A76. doi:10.1051/0004-6361/202140735
- Jung, Y. K., Zang, W., Han, C., et al. 2022, *AJ*, 164, 262. doi:10.3847/1538-3881/ac9c5c
- Kammerer, J., Mérand, A., Ireland, M. J., et al. 2020, *A&A*, 644, A110. doi:10.1051/0004-6361/202038563
- Kervella, P., Bersier, D., Mourard, D., et al. 2004, *A&A*, 428, 587
- Kochanek, C. S., Shappee, B. J., Stanek, K. Z., et al. 2017, *PASP*, 129, 104502. doi:10.1088/1538-3873/aa80d9
- Kos, J., Lin, J., Zwitter, T., et al. 2017, *MNRAS*, 464, 1259. doi:10.1093/mnras/stw2064
- Le Bouquin, J.-B., Berger, J.-P., Lazareff, B., et al. 2011, *A&A*, 535, A67. doi:10.1051/0004-6361/201117586

- Lindegren, L., Klioner, S. A., Hernández, J., et al. 2021a, *A&A*, 649, A2.
doi:10.1051/0004-6361/202039709
- Lindegren, L., Bastian, U., Biermann, M., et al. 2021b, *A&A*, 649, A4.
doi:10.1051/0004-6361/202039653
- Mayor, M., Pepe, F., Queloz, D., et al. 2003, *The Messenger*, 114, 20
- Mérand, A. 2022, *Proc. SPIE*, 12183, 121831N.
doi:10.1117/12.2626700
- Mróz, P., Dong, S., Mérand, A., et al. 2024, *ApJin press*, arXiv:2409.12227
- Onken, C. A., Wolf, C., Bessell, M. S., et al. 2024, *PASA*, 41, e061. doi:10.1017/pasa.2024.53
- Paczynski, B. 1986, *ApJ*, 304, 1.
doi:10.1086/164140
- Piskunov, N. & Valenti, J. A. 2017, *A&A*, 597, A16. doi:10.1051/0004-6361/201629124
- Rattenbury, N. J., & Mao, S. 2006, *MNRAS*, 365, 792
- Recio-Blanco, A., de Laverny, P., Palicio, P. A., et al. 2023, *A&A*, 674, A29.
doi:10.1051/0004-6361/202243750
- Refsdal, s. 1966, *MNRAS*, 134, 315
- Riello, M., De Angeli, F., Evans, D. W., et al. 2021, *A&A*, 649, A3.
doi:10.1051/0004-6361/202039587
- Rybicki, K. A., Wyrzykowski, L., Bachelet, E., et al. 2022, *A&A*, 657, A18.
doi:10.1051/0004-6361/202039542
- Schechter, P. L., Mateo, M., & Saha, A. 1993, *PASP*, 105, 1342. doi:10.1086/133316
- Shappee, B. J., Prieto, J. L., Grupe, D., et al. 2014, *ApJ*, 788, 48.
doi:10.1088/0004-637X/788/1/48
- Sheinis, A., Anguiano, B., Asplund, M., et al. 2015, *Journal of Astronomical Telescopes, Instruments, and Systems*, 1, 035002.
doi:10.1117/1.JATIS.1.3.035002
- Skowron, J., Udalski, A., Gould, A., et al. 2011, *ApJ*, 738, 87. doi:10.1088/0004-637X/738/1/87
- Skrutskie, M. F., Cutri, R. M., Stiening, R., et al. 2006, *AJ*, 131, 1163. doi:10.1086/498708
- Smith, M. C., Mao, S., & Paczyński, B. 2003, *MNRAS*, 339, 925.
doi:10.1046/j.1365-8711.2003.06183.x
- Ting, Y.-S., Conroy, C., Rix, H.-W., et al. 2019, *ApJ*, 879, 69. doi:10.3847/1538-4357/ab2331
- Yee, J. C., Shvartzvald, Y., Gal-Yam, A., et al. 2012, *ApJ*, 755, 102.
doi:10.1088/0004-637X/755/2/102
- Yoo, J., DePoy, D. L., Gal-Yam, A., et al. 2004, *ApJ*, 603, 139. doi:10.1086/381241
- van Cittert, P. H. 1934, *Physica*, 1, 201.
doi:10.1016/S0031-8914(34)90026-4
- Wyrzykowski, L., Kruszyńska, K., Rybicki, K. A., et al. 2023, *A&A*, 674, A23.
doi:10.1051/0004-6361/202243756
- Zang, W., Dong, S., Gould, A., et al. 2020, *ApJ*, 897, 180. doi:10.3847/1538-4357/ab9749
- Zernike, F. 1938, *Physica*, 5, 785.
doi:10.1016/S0031-8914(38)80203-2
- Zhu, W., Penny, M., Mao, S., et al. 2014, *ApJ*, 788, 73. doi:10.1088/0004-637X/788/1/73

Table 1. Best-fit light-curve parameters and 1σ uncertainties

Solution χ^2	t_0 (HJD')	u_0	t_E (days)	ρ	s	q	α (deg)	$\pi_{E,N}$	$\pi_{E,E}$	ds/dt (yr $^{-1}$)	$d\alpha/dt$ (yr $^{-1}$)	β
close A+	9601.24	0.035	65.4	0.056	0.4	0.36	37.4	-0.28	-0.14	0.15	-1.41	0.03
1005.3	+0.04 -0.05	+0.002 -0.002	+1.3 -1.1	+0.002 -0.002	+0.1 -0.1	+0.04 -0.03	+0.6 -0.6	+0.04 -0.03	+0.02 -0.02	+0.02 -0.02	+0.07 -0.06	+0.01 -0.01
close A-	9601.11	-0.028	74.0	0.048	0.4	0.21	-38.1	-0.14	-0.10	0.20	2.11	0.12
1013.5	+0.06 -0.04	+0.002 -0.002	+1.4 -1.8	+0.003 -0.002	+0.1 -0.1	+0.04 -0.02	+0.6 -0.6	+0.03 -0.03	+0.02 -0.02	+0.02 -0.03	+0.05 -0.08	+0.02 -0.03
close B+	9601.35	0.040	63.5	0.056	0.4	0.50	-47.9	-0.27	-0.09	0.16	1.49	0.03
1025.9	+0.03 -0.03	+0.002 -0.002	+0.9 -1.1	+0.002 -0.002	+0.1 -0.1	+0.05 -0.05	+0.5 -0.5	+0.03 -0.02	+0.02 -0.02	+0.01 -0.01	+0.06 -0.06	+0.01 -0.01
wide A+	9601.34	0.035	56.3	0.068	5.4	1.04	33.2	-0.40	-0.03	0.80	0.16	0.98
1028.4	+0.03 -0.04	+0.002 -0.002	+1.4 -1.3	+0.002 -0.003	+0.2 -0.2	+0.08 -0.07	+0.6 -0.5	+0.03 -0.03	+0.02 -0.02	+0.14 -0.15	+0.03 -0.04	+0.02 -0.05
wide A-	9601.30	-0.028	69.5	0.054	5.1	0.77	-38.5	-0.13	-0.24	0.19	-0.11	0.39
948.9	+0.08 -0.07	+0.002 -0.002	+3.0 -3.3	+0.002 -0.002	+0.3 -0.3	+0.09 -0.08	+1.1 -0.9	+0.06 -0.08	+0.02 -0.01	+0.34 -0.33	+0.06 -0.05	+0.31 -0.18
wide B+	9601.07	0.033	61.1	0.054	6.2	1.27	-39.0	-0.22	-0.26	1.03	-0.00	0.87
999.6	+0.04 -0.04	+0.002 -0.002	+1.9 -1.9	+0.003 -0.002	+0.3 -0.3	+0.12 -0.09	+1.1 -1.1	+0.07 -0.07	+0.01 -0.01	+0.07 -0.14	+0.04 -0.03	+0.07 -0.20

NOTE—For close solutions ($s < 1$), t_0 and u_0 are defined relative to the barycenter of the lens system, and the parameters $\{t_E, s, \rho, \pi_{E,N}, \pi_{E,E}\}$ are in units of the θ_E of the total mass. For wide solutions ($s > 1$), t_0 and u_0 are defined relative to the magnification center of the primary lens (Dong et al. 2006), and the parameters $\{t_E, s, \rho, \pi_{E,N}, \pi_{E,E}\}$ are defined in units of the θ_E of the primary lens. The favored solution “wide A-” is in boldface.

Table 2. Best-fit parameters and 1σ uncertainties from the joint VLTI and light-curve analysis

Solution χ^2	t_0 (HJD')	u_0	t_E (days)	ρ	s	q	α (deg)	π_E	ds/dt (yr $^{-1}$)	$d\alpha/dt$ (yr $^{-1}$)	β	θ_E (mas)	Ψ (deg)
close A-	9601.14	-0.027	74.4	0.051	0.4	0.23	-37.4	0.18	0.18	2.09	0.10	0.737	258.6
1220.0	+0.02 -0.02	+0.001 -0.001	+0.7 -0.6	+0.001 -0.001	+0.1 -0.1	+0.01 -0.01	+0.4 -0.4	+0.01 -0.01	+0.01 -0.01	+0.02 -0.03	+0.01 -0.01	+0.002 -0.002	+0.2 -0.2
wide A-	9601.12	-0.028	70.1	0.058	4.1	0.51	-40.0	0.35	-0.78	-0.09	0.47	0.724	259.4
1174.8	+0.04 -0.04	+0.001 -0.001	+1.1 -0.9	+0.001 -0.001	+0.1 -0.1	+0.03 -0.03	+0.5 -0.5	+0.02 -0.01	+0.20 -0.18	+0.03 -0.03	+0.23 -0.17	+0.002 -0.002	+0.2 -0.2
wide B+	9600.68	-0.005	63.9	0.062	4.2	0.76	-53.0	0.46	0.49	-0.14	0.26	0.726	262.5
1470.5	+0.03 -0.03	+0.001 -0.001	+1.1 -1.2	+0.001 -0.001	+0.1 -0.1	+0.01 -0.01	+0.5 -0.6	+0.02 -0.02	+0.20 -0.20	+0.04 -0.04	+0.07 -0.06	+0.002 -0.002	+0.2 -0.2

NOTE—The light-curve parameters are defined in the same fashion as in Table 1. For wide solutions, θ_E is defined by the mass of the primary lens, while for close solutions, it is defined by the total mass of the lens system. The favored solution “wide A-” is in boldface.

Table 3. Derived physical parameters of the lens system

M_1 (M_\odot)	M_2 (M_\odot)	r_\perp (au)	π_{rel} (mas)	D_L (kpc)	$\mu_{\text{hel,N}}$ (mas yr $^{-1}$)	$\mu_{\text{hel,E}}$ (mas yr $^{-1}$)
$0.256^{+0.008}_{-0.006}$	$0.130^{+0.007}_{-0.007}$	$6.83^{+0.31}_{-0.27}$	$0.251^{+0.007}_{-0.007}$	$2.29^{+0.08}_{-0.08}$	$-1.36^{+0.05}_{-0.05}$	$-2.66^{+0.06}_{-0.05}$

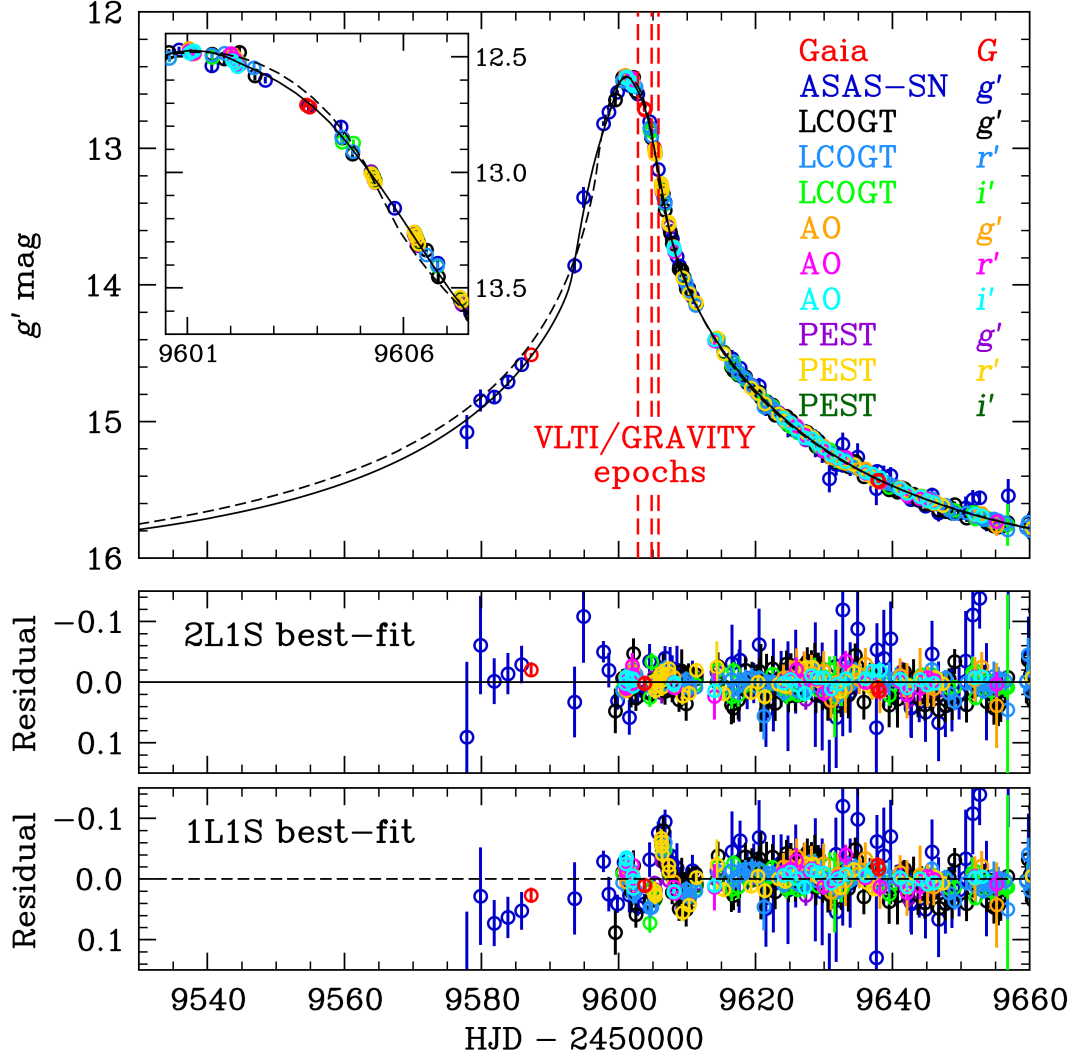


Figure 1. Top: the multiband light curves of the microlensing event ASASSN-22av, which are well described by the best-fit 2L1S model (black solid line) from the joint VLTI and light-curve analysis. The light curves deviate from the best-fit 1L1S model with finite-source effects (black dashed line) near the peak, as shown with the enlarged view in the inset. We analyze three nights of VLTI GRAVITY observations taken after the peak, and their epochs are marked with the red dashed lines. Middle: the residuals of the best-fit 2L1S model. Bottom: the best-fit 1L1S model shows significant residuals for the ~ 10 days around the peak.

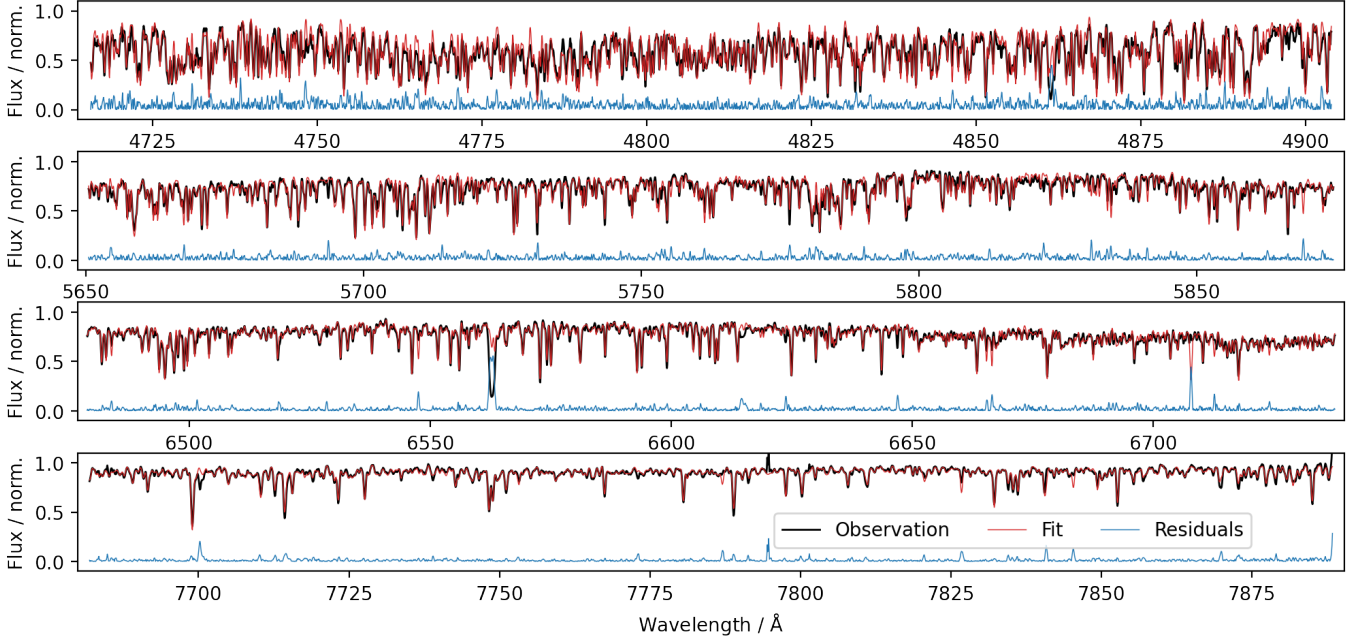


Figure 2. The observed (black) and fitted (red) synthetic HERMES spectra from GALAH DR4, showing generally good agreement and small residuals (blue) across the entire spectrum. While some individual lines are deviating, the overall fit is well aligned with the observations, whose continuum is suppressed by molecular absorption features across the entire wavelength region of this luminous cool giant star.

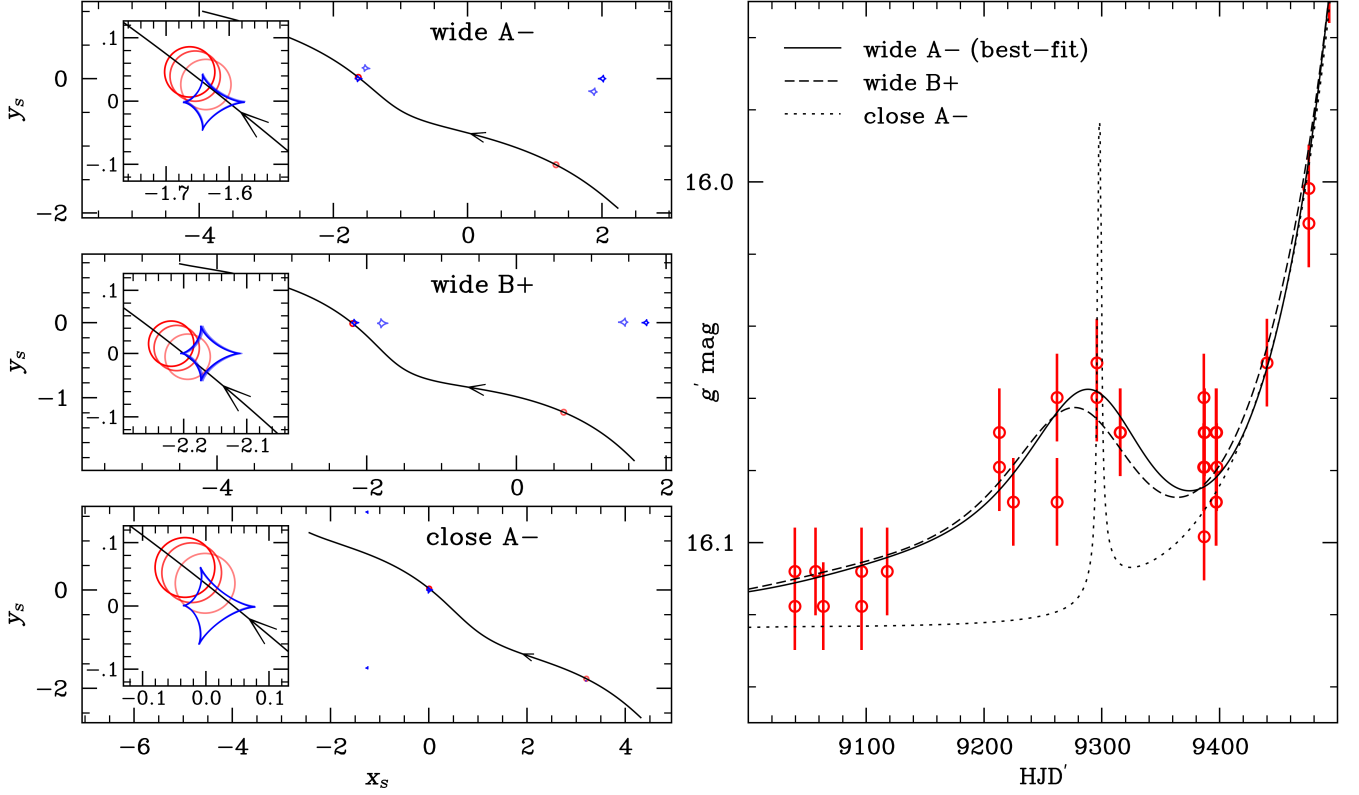


Figure 3. The source trajectories and light curves of three 2L1S models (“wide A–”, “wide B+”, and “close A–”) taking the microlens parallax and binary orbital motion into account. Left: the upper, middle, and lower subpanels show the caustics (blue) and source trajectories (black curves with arrows) for the “wide A–” (best-fit), “wide B+”, and “close A–” solutions, respectively. In each subpanel, we show the source positions (red circles) and caustics at $\text{HJD}' = 9300$ and 9601 , with increased opacity for the latter. The inset of each subpanel displays the source positions and caustics on the three nights of the VLTi GRAVITY observations. Right: the Gaia G -band light curve shows a broad feature at $\text{HJD}' \sim 9300$, and the three best-fit 2L1S models are shown with solid (wide A–), dashed (wide B+), and dotted (close A–) lines, respectively. The wide solutions can match this feature well, while the “close A–” solution cannot. The sharply peaked spike of the “close A–” solution is induced by the source crossing a planetary caustic due to dramatic orbital motions, but even this finely tuned configuration fails to reproduce the observed feature.

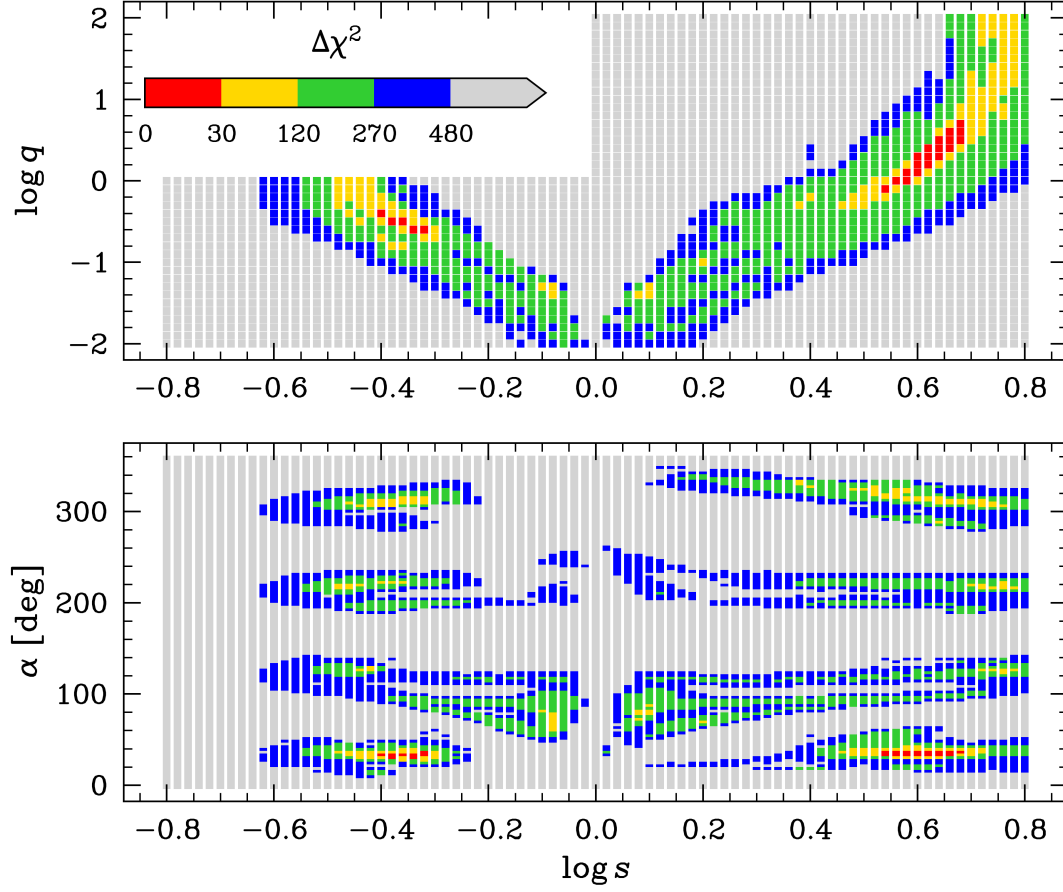


Figure 4. $\Delta\chi^2$ map for the grid search of 2L1S light-curve models, in the $\log s - \log q$ (upper panel) and $\log s - \alpha$ (lower panel) planes. For $\log s < 0$, there is a perfect degeneracy $(\log q, \alpha) \rightarrow (-\log q, \alpha + \pi)$, and thus the search is only conducted with $\log q \leq 0$. The regions with $\Delta\chi^2 < 30, 120, 270, 480$, and > 480 with respect to the best fit are color-coded with red, yellow, green, blue, and light gray, respectively.

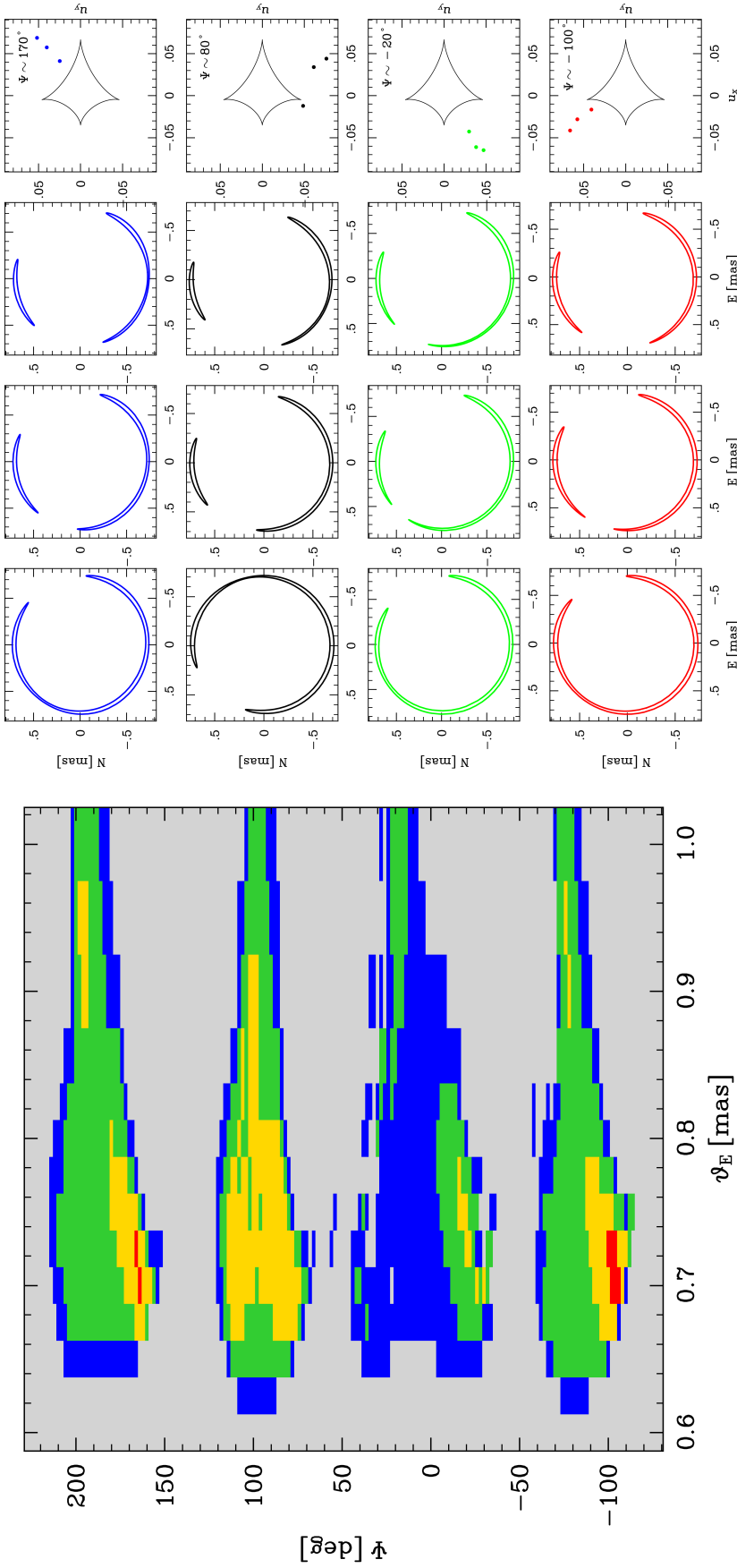


Figure 5. Left: the $\Delta\chi^2_{\text{tot}}(\theta_E, \Psi)$ map from fitting the VLTI data evaluated at $(s, q, \rho) = (3.8, 0.84, 0.044)$. Areas with $\Delta\chi^2 < 30, 120, 270, 480$, and $\Delta\chi^2 > 480$ are color-coded in red, yellow, green, blue, and gray, respectively. There are four local minima around $\Psi = (170^\circ, 80^\circ, -10^\circ, -100^\circ)$. Right: images and geometry of the four local minima. The four rows from top to bottom correspond to local minima at $\Psi = 170^\circ$ (blue), 80° (black), -10° (green), and -100° (red), respectively. The first three columns show the model images oriented in the east and north directions on the three VLTI nights. The last column shows the source positions (solid dots) on the three VLTI nights and the caustics (black closed curve).

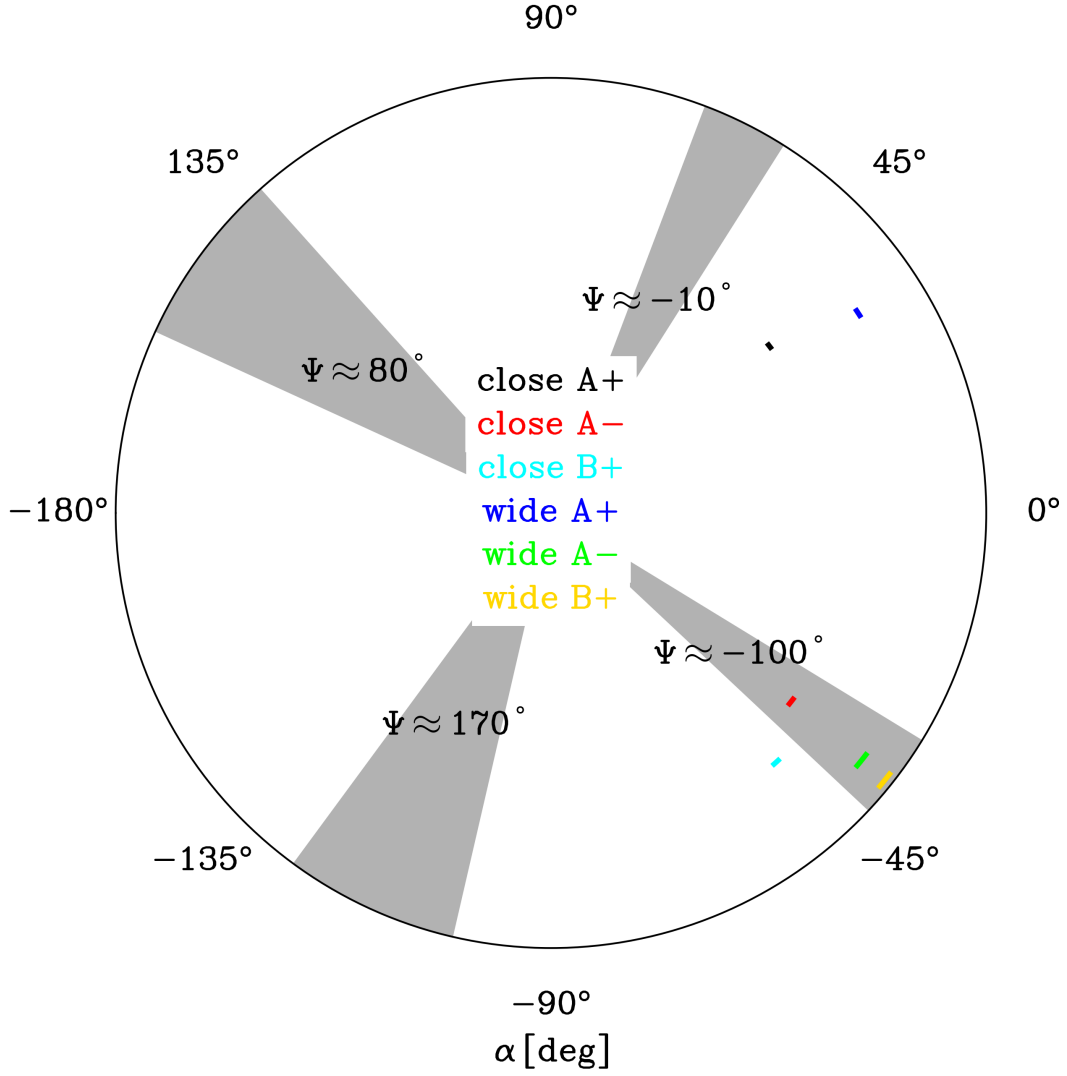


Figure 6. The comparisons of α_{LC} derived from light-curve fitting with α_{VLTI} inferred from VLTI data. The colored arcs denote the 1σ range of α_{LC} for the solutions “close A+” (black), “close A−” (red), “close B+” (cyan), “wide A+” (blue), “wide A−” (green), and “wide B+” (yellow), respectively. The shaded regions indicate the 3σ range of α_{VLTI} at $\Psi \sim -100^\circ, -10^\circ, 80^\circ$, and 170° . Three solutions (“wide A−”, “wide B+” and “close A−”) have consistent α_{LC} with α_{VLTI} .

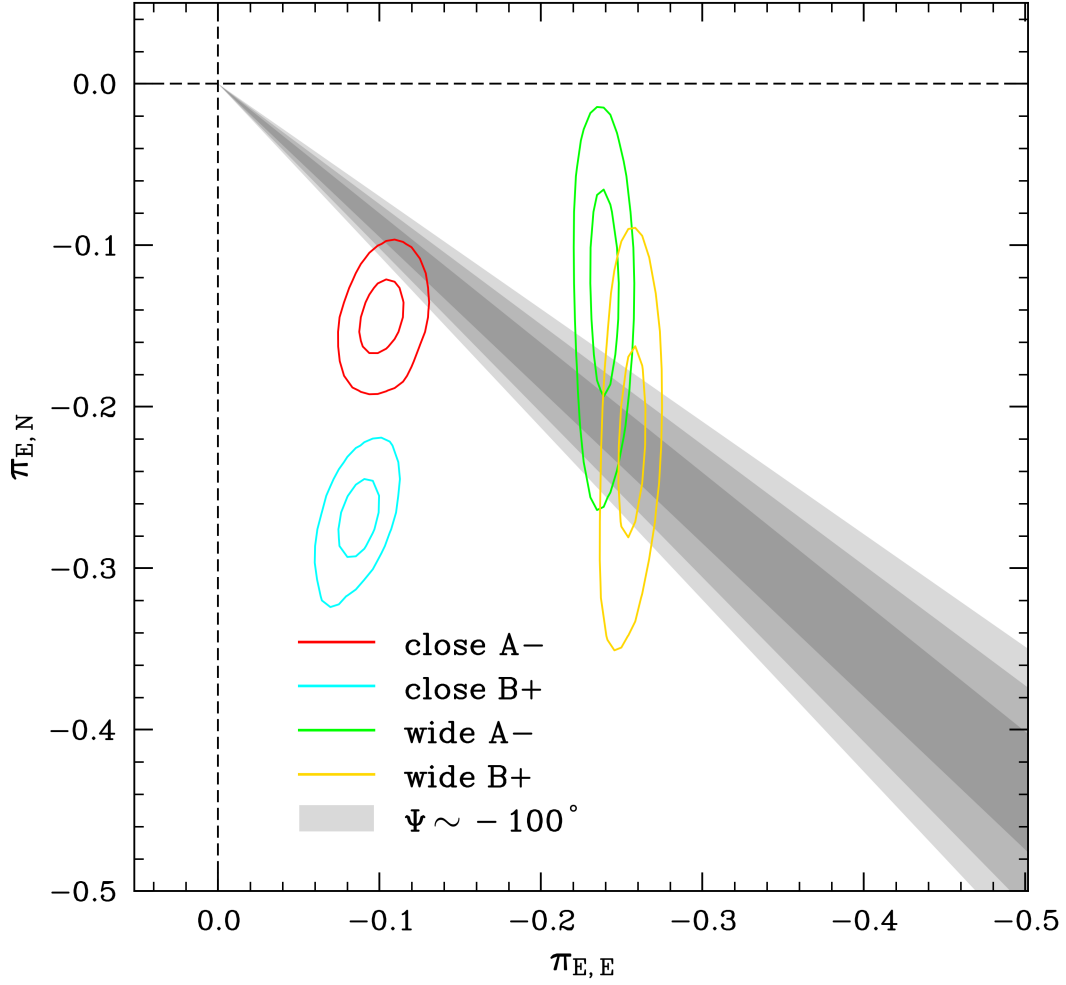


Figure 7. The 1 and 2 σ posterior distributions of the microlens parallax vector $\pi_E = (\pi_{E,E}, \pi_{E,N})$ from light-curve analysis for the “close A+” (red contours), “close B+” (cyan contours), “wide A−” (green contours), and “wide B+” (yellow contours) solutions, respectively. The shaded regions are the 1 σ , 2 σ , and 3 σ constraints on Φ_π derived from the interferometric data for the local minimum of $\Psi \sim -100^\circ$. The light-curve and VLTI constraints are consistent for the “wide A−”, “wide B+” and “close A−” solutions.

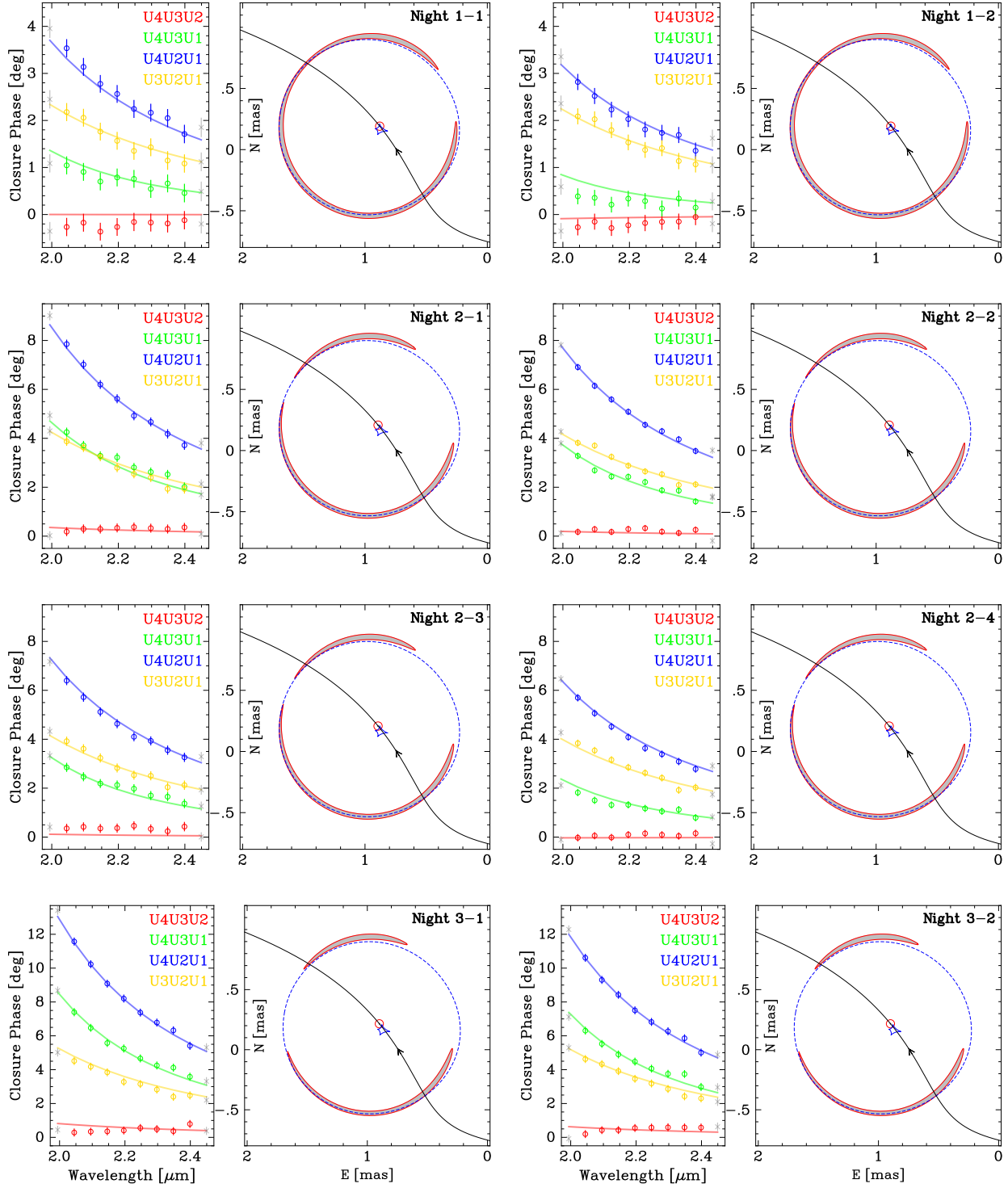


Figure 8. Four \times two panel groups showing the closure-phase data and the best-fit microlensing model (“wide A–”) for the eight VLT GRAVITY exposures obtained over three nights. Within each group, the left subpanel shows the closure-phase data as a function of wavelength, with the best-fit model overplotted as solid lines; the right subpanel shows the caustics (blue), source trajectory (black line with an arrow), and source position (red circle) at the time of the VLT observation, with the microlensed images displayed as shaded regions and the critical curves as blue dashed lines.

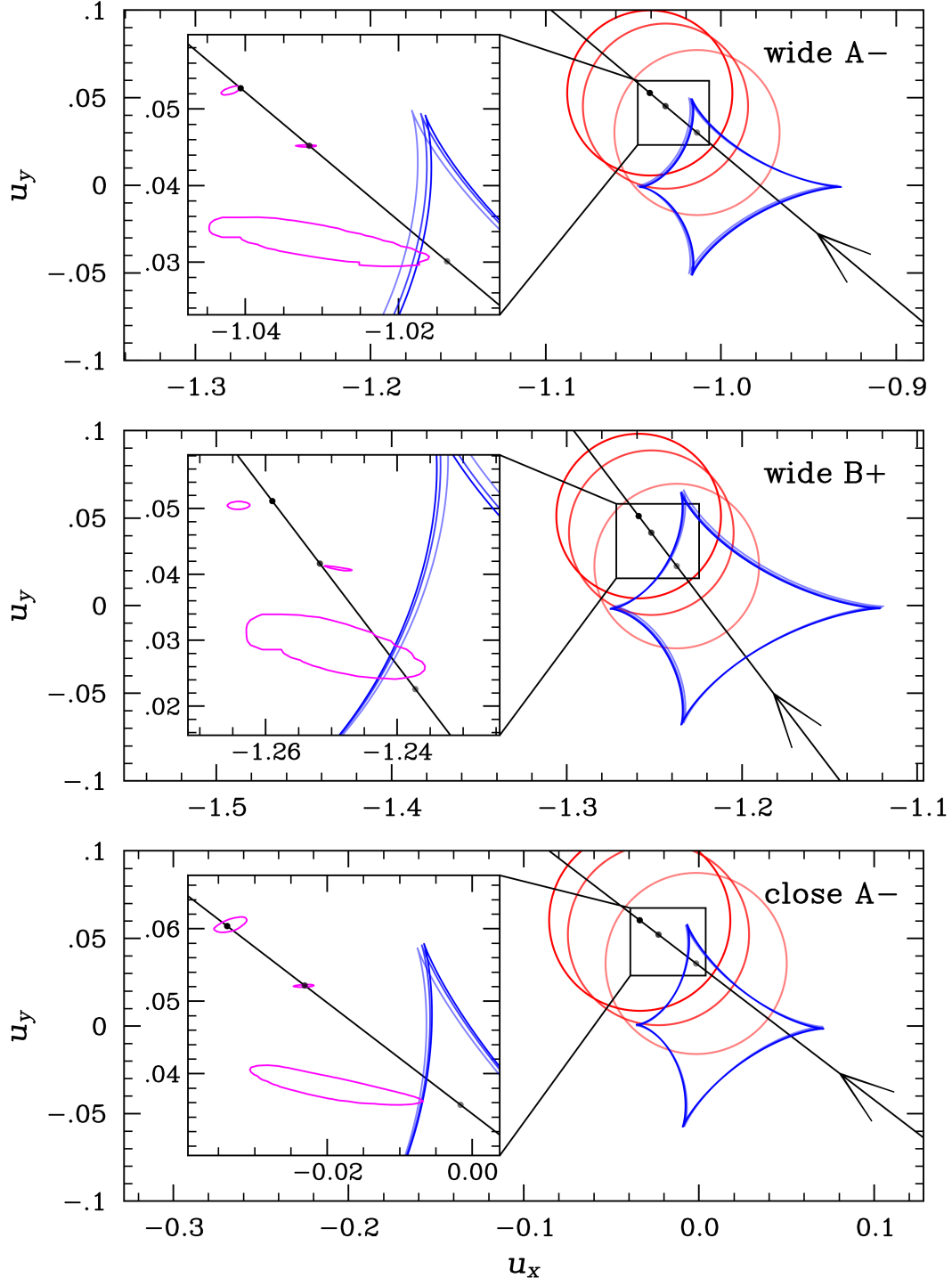


Figure 9. The source trajectory (black solid line) and caustics (blue closed curves) for “wide A-” (top panel), “wide B+” (middle panel), and “close A-” (bottom panel) solutions. The solid dots denote the source positions on the three nights of VLT/ GRAVITY observations. The 3σ contours in magenta show the posteriors of the source positions inferred from the interferometric data only, with the geometric parameters ($s, q, \rho, \theta_E, \Psi$) held fixed to the values in Table 2.